

Low volcanic outgassing rates for a stagnant lid Archean Earth with graphite-saturated magmas

Claire Marie Guimond^{a,b,*}, Lena Noack^a, Gianluigi Ortenzi^{a,c}, Frank Sohl^c

^a*Freie Universität Berlin, Institute of Geological Sciences, Malteserstrasse 74-100, 12249 Berlin, Germany*

^b*Bullard Laboratories, Department of Earth Sciences, University of Cambridge, Madingley Rise, Cambridge CB3 0EZ, UK*

^c*German Aerospace Centre, Institute of Planetary Research, Rutherfordstrasse 2, 12489 Berlin, Germany*

Abstract

Volcanic gases supplied a large part of Earth’s early atmosphere, but constraints on their flux are scarce. Here we model how C-O-H outgassing could have evolved through the late Hadean and early Archean, under the conditions that global plate tectonics had not yet initiated, all outgassing was subaerial, and graphite was the stable carbon phase in the melt source regions. The model fully couples numerical mantle convection, partitioning of volatiles into the melt, and chemical speciation in the gas phase. The mantle oxidation state (which may not have reached late Archean values in the Hadean) is the dominant control on individual species’ outgassing rates because it affects both the carbon content of basaltic magmas and the speciation of degassed volatiles. Volcanic gas from mantles more reduced than the iron-wüstite mineral redox buffer would contain virtually no CO₂ because (i) carbonate ions dissolve in magmas only in very limited amounts, and (ii) almost all degassed carbon takes the form of CO instead of CO₂. For oxidised mantles near the quartz-fayalite-magnetite buffer, we predict median CO₂ outgassing rates of less than approximately 5 Tmol yr⁻¹, still lower than the outgassing rates used in many Archean climate studies. Relatively weak outgassing is due in part to the redox-limited CO₂ contents of graphite-saturated melts, and also to a stagnant lid regime’s inefficient replenishment of upper mantle volatiles. Our results point to certain chemical and geodynamic prerequisites for sustaining a clement climate with a volcanic greenhouse under the Faint Young Sun.

Keywords: outgassing, secondary atmospheres, mantle redox, early Earth, planetary dynamics, mantle convection, numerical modelling

1. Introduction

The Hadean-Archean atmosphere cloaked the only environment in the universe known to support the origin of life. This atmosphere would have been fed by volatile chemicals outgassed from the interior (Holland, 1984; Kasting et al., 1993; Gaillard and Scaillet, 2014), as well as extraterrestrial impacts (Zahnle et al., 2020) and perhaps a lingering, degassed magma ocean atmosphere (Katyál et al., 2020). Yet hardly any observable record of the Archean atmosphere remains. Our knowledge surrounding its makeup rests on modelling. Mantle outgassing models lend boundary conditions to the processes controlling the atmospheric composition and planetary climate. However, predictions from these models are very much entwined with certain assumptions—in particular, the tectonic regime and oxidation state of the mantle. Archean outgassing scenarios hinging on mobile plates and an oxidised mantle form the basis of contemporaneous climate studies (e.g., Sleep and Zahnle, 2001). This work offers an alternative to these recurring premises: a fully-coupled numerical estimation of the volcanic outgassing rates of CO₂, CO, H₂O, and H₂, for a stagnant lid Earth under a range of mantle oxidation states.

*Corresponding author

Email address: cmg76@cam.ac.uk (Claire Marie Guimond)

The oxidation state of the upper mantle controls the chemical speciation of volcanic gas. Increasing the mantle’s oxygen fugacity, f_{O_2} , raises the ratio of oxidised to reduced volatile species in the melt phase: $[\text{CO}_2]/[\text{CO}]$ and $[\text{H}_2\text{O}]/[\text{H}_2]$ in the C-O-H system (Holland, 1984). As the melt rises adiabatically through conduits, its f_{O_2} re-equilibrates with the decreasing pressure; gas abundances at the surface are also linked to the mantle source region (Kasting et al., 1993). On modern Earth, for example, the dominant species in volcanic gas are H_2O and CO_2 , in line with a mantle source f_{O_2} in equilibrium with the quartz-fayalite-magnetite (QFM) mineral buffer (Holland, 1984).

Besides the effect of f_{O_2} on volatile speciation, there can be a compounding redox control on the partitioning of carbon into the melt. This effect becomes relevant when graphite is the stable carbon phase in the upper mantle. During melting, carbonate ions are produced from a reaction of graphite with oxygen via CO_2 (Holloway et al., 1992). The total carbon outgassing flux depends on how much carbon (as CO_3^{2-}) can dissolve into the melt.

Although these two redox effects are well-known, the value itself of the Archean mantle f_{O_2} remains weakly constrained at best. Immediately after core formation, the magma ocean must have been reduced (Wood et al., 2006). Meanwhile, scant geological evidence suggests that by ~ 3.8 Ga at the latest, the uppermost mantle was already about as oxidised as today (Canil, 1997; Delano, 2001; Trail et al., 2011; Nicklas et al., 2019; Armstrong et al., 2019). Yet uncertainty persists on the timing of this oxidation (see section 2.5.3). Therefore, to cover the possible spread of redox states, we investigate outgassing fluxes under a wide range of mantle f_{O_2} , especially in proportion to other unknown parameters such as the mantle volatile content and thermal state.

Whilst this study is set up to explore many redox scenarios, it will be limited to one tectonic regime. For this we consider the end-member case of stagnant lid convection (Debaille et al., 2013). The possibility of a stagnant lid regime appears underexplored in early Earth climate studies, despite the ambiguity around plate tectonics’ operation through the Archean (e.g., Brown et al., 2020); as such we hope to complement other work assuming a mobile lid. This modelling decision is important because mobile lids may be associated with much higher outgassing rates than stagnant lids (Noack et al., 2014, 2017). The mechanistic explanations are not straightforward—being a combination of competing effects discussed later in section 4.1.5—and would benefit from dedicated work in the future.

By numerically coupling mantle convection, redox-dependent melt partitioning of volatiles, and redox-dependent speciation, and by investigating a broader range of mantle oxidation states, we can advance the current literature dedicated to C-O-H outgassing from solid-state mantles of rocky planets in the solar system and elsewhere (O’Neill et al., 2007; Grott et al., 2011; Noack et al., 2014, 2017; Tosi et al., 2017; Dorn et al., 2018; Ortenzi et al., 2020). Previous studies have tended to assume an oxidising mantle, akin to that of present-day Earth—exceptions include Grott et al. (2011) for the reduced early Mars, and Tosi et al. (2017), Ortenzi et al. (2020), and Liggins et al. (2020) for fiducial rocky exoplanets. Further, numerical convection carries the advantage of resolving the local temperatures and pressures of melt parcels, to which f_{O_2} is very sensitive.

An approach parallel to the one taken here is to parameterise outgassing fluxes in terms of melt production (e.g., Sleep and Zahnle, 2001; Papuc and Davies, 2008; Kite et al., 2009; Kadoya and Tajika, 2015; Foley and Driscoll, 2016; Charnay et al., 2017; Krissansen-Totton et al., 2018; Foley and Smye, 2018; Krissansen-Totton and Catling, 2020). In parameterised models, mantle melting rates are often scaled to an estimate of the interior heat flux. Past outgassing rates can then be calibrated to present-day estimates. These types of outgassing parameterisations may imply higher outgassing fluxes than do numerical convection models for two reasons. Firstly, heat flow scalings extrapolated backwards in time will necessarily lead to higher-than-modern outgassing rates because parameterised thermal history models predict high heat flow early in a planet’s evolution (e.g., Turcotte, 1980). Secondly, 1D models tend to overestimate melt fractions early in a planet’s thermal evolution, since they cannot spatially resolve depletion upon partial melting—local depletion would inhibit further local melting for the same temperature. In addition to these systematic effects, applying a single scaling relationship assumes no change in mantle oxidation state or tectonic regime.

Planetary outgassing rates require attention because they lie at the core of at least two unsolved Archean mysteries. The first is that reduced gases such as H_2 and CO may be necessary for prebiotic chemistry. The production of HCN requires a reducing atmosphere with $\text{C}/\text{O} \geq 1$, for example (Rimmer et al., 2019). How-

ever, whether H₂ and CO could have comprised a significant part of volcanic gas at the time remains debated (e.g., Zahnle et al., 2020). The second mystery is that sufficiently large partial pressures of greenhouse gases seem required to incubate early Earth under lower solar luminosity (Charnay et al., 2020) and make sense of liquid surface water (Sagan and Mullen, 1972). Although no solution to this paradox has emerged as the likely favourite, most atmospheric evolution scenarios proposed so far rely on CO₂ outgassing fluxes at least as high as the present day (e.g., Sleep and Zahnle, 2001; Wordsworth and Pierrehumbert, 2013; Kanzaki and Murakami, 2018). Neither of these two driving questions may ever be resolvable without definite constraints on the timing of mantle oxidation, or plate tectonics’ initiation. Nevertheless, this study, by more rigorously linking stagnant lid outgassing fluxes to the unknown oxidation state, might help contextualise these problems within Earth system evolution.

2. Methods

We trace the movement of volatiles through the mantle to the atmosphere for a stagnant-lid Earth, from just after the moon-forming impact to around the first rock record. Our model is similar to the one described in Ortenzi et al. (2020), who additionally calculated gas solubility in the melt (relevant for the higher outgassing pressures expected on exoplanets greater than an Earth mass), but coupled partitioning and volatile speciation *a posteriori* within the convection simulations, rather than directly.

To simulate mantle dynamics, we use a 2D convection model, which is detailed in Noack et al. (2016). The heavily-benchmarked model couples solid-state convection in the mantle with spatially-resolved melt fractions and volatile partitioning in the melt (Holloway et al., 1992; Katz et al., 2003; Grott et al., 2011). This is further coupled with a chemical speciation model (French, 1966; Holloway, 1981; Fegley, 2013; Gailard and Scaillet, 2014; Schaefer and Fegley, 2017). At each time step the model produces outgassed masses of H₂O, H₂, CO₂, and CO. We simulate 700 Myr of convection, with time-zero nominally corresponding to 4.5 Ga.

2.1. Numerical convection model

The convection code solves the conservation equations of mass, momentum and energy in the rocky mantle by using a particle-in-cell method. We use the 2D spherical annulus method in Hernlund and Tackley (2008) to divide the mantle into a mesh of cells with an average lateral and radial resolution of 50 km between grid points. The radial resolution coarsens linearly with depth, varying from 10 km at the surface to 90 km at the core-mantle boundary. To reduce computational costs, we model one quarter of the 2D annulus, corresponding to 307 cells in the lateral direction. We found that minor changes in resolution did not affect degassing.

We model compressible convection based on the truncated anelastic liquid approximation (TALA), using pre-calculated depth-dependent profiles for thermodynamic parameters such as the mineral-dependent density, the thermal expansion coefficient and the heat capacity for an adiabatic temperature profile. We neglect any possible initiation of plate tectonics or other surface recycling mechanisms and instead allow for a stagnant lid to form.

We take into account time-dependent radiogenic heating and heat loss from the core. The radiogenic heat sources decline over time and would reach present-day Earth values of 79.5 ppb Th, 240 ppm K and 20.3 ppb U after 4.5 Gyr of thermal evolution, following Schubert et al. (2001). We did not include the partitioning of heat sources in the crust, and instead applied homogeneous radiogenic heat sources over the entire domain.

We assume a hydrated pyrolitic mantle with an Arrhenius viscosity, η , that depends on the local temperature T and pressure p , following Karato and Wu (1993):

$$\eta(T, p) = \frac{1}{2A} d^r \exp\left(\frac{E + pV}{RT}\right), \quad (1)$$

with, for the upper mantle, a prefactor $A = 3.7 \times 10^{-19} \text{ m}^{-r} \text{ Pa}^{-1} \text{ s}^{-1}$, grain size $d = 1 \text{ mm}$, grain size exponent $r = 2.5$, activation energy $E = 240 \text{ kJ mol}^{-1}$, and activation volume $V = 5.0 \text{ cm}^3 \text{ mol}^{-1}$, where R

is the gas constant. The lower mantle rheology behaves as in Noack et al. (2017), with a viscosity prefactor and pressure-dependent activation enthalpy following Tackley et al. (2013); that is, V decreases with pressure in the lower mantle. Whereas Tackley et al. (2013) increased their viscosities by a factor of 100 to allow for numerically-feasible simulations, we do not also adopt this scale factor, so the lower mantle is less viscous compared to their study.

Whilst we model a wet mantle, we do not consider local viscosity variations due to heterogeneous water contents. We do not implement an aesthenosphere, and may underestimate the convective strength locally in the upper mantle. Our initial Rayleigh number, estimated for a global average viscosity of about 10^{21} Pa s, is around 5×10^7 . However, depending on the initial temperature profile and its local variations, the viscosity can be much lower than this—especially in the upper mantle—permitting more vigorous convection in some regions.

2.2. Melting model

The petrological model simulates partial melting of the silicate mantle. Melt forms if the local temperature is greater than the mantle solidus temperature, T_{solidus} , at that temperature and pressure. The local melt fraction, F , is

$$F = \frac{T - T_{\text{solidus}}}{T_{\text{liquidus}} - T_{\text{solidus}}}. \quad (2)$$

The solidus and liquidus parameterisations, given in Noack et al. (2014), are fits to experimental data for peridotite melting valid up to 15 GPa (De Smet, 1999). The liquidus temperature, T_{liquidus} , is constant for a given pressure. The solidus temperature decreases with water content in the melt (Katz et al., 2003), and increases upon depletion due to prior melting. Melting also consumes latent heat, feeding back into the local mantle temperatures. We assume that the upper mantle melt is buoyant only at pressures of less than 12 GPa (Ohtani et al., 1995), hence we neglect any contribution from melting at greater depths.

The local melt fractions add up to give the total chemical depletion of the mantle. Here, depletion is adapted to the fact that dehydration increases the solidus temperature. We recalculate the depletion at each time step using the updated solidus temperature. Upon 30% depletion of the primordial peridotite mantle, the residual mantle therefore always resembles the harzburgite composition, independently of if it having started wet or dry. Depletion is limited to 30%. We do not consider density variations in the mantle residue upon melting; that is, there is no buoyancy effect due to depletion.

2.3. Volatile partitioning model

At each time step, if the local melt fraction is greater than zero, we calculate the amounts of C and H_2O that enter the melt phase, and subtract them from the local chemical inventories. These inventories (as well as other local information such as the depletion) are traced via mass-independent particles that flow along convective stream lines. We ensure that each cell, which is fixed in space, has between 3 and 8 particles. No local partitioning occurs once a particle’s volatile inventory is emptied; if a particle is dehydrated, it remains so. As the mantle convects, however, cells can be replenished by fresh particles rising up from the lower mantle, which replace the dehydrated particles.

Carbon dissolves into the melt as CO_3^{2-} ; its mole fraction, $X_{\text{CO}_3^{2-}}^{\text{melt}}$, depends strongly on f_{O_2} :

$$X_{\text{CO}_3^{2-}}^{\text{melt}} = \frac{K_{\text{I}} K_{\text{II}} f_{\text{O}_2}}{1 + K_{\text{I}} K_{\text{II}} f_{\text{O}_2}}, \quad (3)$$

where K_{I} and K_{II} are the equilibrium constants governing, respectively, the formation of CO_2 from graphite and CO_3^{2-} from CO_2 ,

$$\log_{10} K_{\text{I}} = a - bT + cT^2 + d \frac{p-1}{T} \quad (4)$$

$$\log_{10} K_{\text{II}} = e - \frac{f}{T} - g \frac{p-1000}{T}, \quad (5)$$

Table 1: Thermodynamic parameters for basaltic melt.

SYMBOL	DESCRIPTION	VALUE	UNITS	REFERENCE
α_{melt}	Thermal expansion coefficient	3×10^{-5}	K^{-1}	Afonso et al. (2005)
ρ_{melt}	Density	3000	kg m^{-3}	Lesher and Spera (2015)
$C_{p,\text{melt}}$	Heat capacity	1793	$\text{J kg}^{-1} \text{K}^{-1}$	Lesher and Spera (2015)

where $a = 40.07639$, $b = 2.53932 \times 10^{-2}$, $c = 5.27096 \times 10^{-6}$, $d = 0.0267$, $e = -6.24763$, $f = 282.56$, $g = 0.119242$, T is in K, and p is in bar (Holloway et al., 1992; Grott et al., 2011; Hirschmann and Withers, 2008).

The amount of CO_2 in weight percent, here denoted χ to distinguish from mole percent, is calculated from $X_{\text{CO}_3^{2-}}^{\text{melt}}$, assuming thermodynamic equilibrium:

$$\chi_{\text{CO}_2}^{\text{melt}} = \left[\frac{M_{\text{CO}_2}}{\text{FWM}} X_{\text{CO}_3^{2-}}^{\text{melt}} \right] / \left[1 - \left(1 - \frac{M_{\text{CO}_2}}{\text{FWM}} \right) X_{\text{CO}_3^{2-}}^{\text{melt}} \right], \quad (6)$$

where M_{CO_2} is the molar mass of carbon dioxide in g mol^{-1} and FWM is the formula weight of the melt normalised to one oxygen, equal to $36.594 \text{ g mol}^{-1}$ for an example tholeiitic basaltic (Holloway et al., 1992; Grott et al., 2011). The formula weight typically varies only by few percent for different basalt compositions. Note that although (3–6) do not directly involve the mantle source concentration, $\chi_{\text{CO}_2}^{\text{melt}}$ is capped at the source concentration locally.

We assume that all solid carbon exists as graphite, since we only consider shallow melting below 12 GPa. This assumption may not be valid for the most oxidised cases (IW + 4), as carbonate may become the stable carbon species for these pressures and f_{O_2} (Stagno, 2019). However, in such oxidised conditions we already know that CO_2 is outgassed, and neglect any carbonate stability.

For water partitioning, we use the batch melting formula:

$$\chi_{\text{H}_2\text{O}}^{\text{melt}} = \frac{\chi_{\text{H}_2\text{O}}^{\text{rock}}}{D_{\text{H}_2\text{O}} + F(1 - D_{\text{H}_2\text{O}})}, \quad (7)$$

where $\chi_{\text{H}_2\text{O}}^{\text{rock}}$ is the local weight fraction of water in the solid mantle, F is the local average melt fraction, and $D_{\text{H}_2\text{O}}$ is a partition coefficient, which we set at 0.01 based on the Ce partitioning coefficient (Michael, 1995; Katz et al., 2003).

Whilst the melt rises adiabatically towards the surface, we only allow a fixed fraction of the melt, χ_{extr} , to reach the surface as extrusive volcanism. Only this extrusive melt contributes to outgassing into the atmosphere. The mantle volatile concentrations are small enough to not saturate (Katz et al., 2003). We do not consider submarine degassing, so virtually all gas molecules enter the atmosphere at these lower surface pressures. Our model therefore assumes complete outgassing of the melt that reaches the surface, with no residual volatiles remaining in the melt. Finally, we do not consider any possible re-equilibration or contamination as material rises through the lithosphere, and neglect whether the melt interacts with the surrounding rock or with fluids at higher pressures.

2.4. Volatile speciation model

We retrieve the masses of outgassed volatiles using the ‘‘Equilibrium constants and mass balance method’’ first appearing in French (1966), and used widely in other studies (Holland, 1984; Gaillard and Scaillet, 2014; Fegley, 2013; Schaefer and Fegley, 2017; Ortenzi et al., 2020). The $[\text{H}_2]/[\text{H}_2\text{O}]$ and $[\text{CO}]/[\text{CO}_2]$ molar ratios are governed by the chemical equilibria,



assuming that the volcanic gases are in equilibrium with their magmas. These chemical reactions have respective equilibrium constants K_{III} and K_{IV} , which are calculated as follows:

$$K_{\text{III}} = \exp\left(\frac{-\Delta_r G_{(8)}^0}{RT}\right) = \frac{(X_{\text{H}_2\text{O}})^2}{(X_{\text{H}_2})^2 f_{\text{O}_2}}, \quad (10)$$

$$K_{\text{IV}} = \exp\left(\frac{-\Delta_r G_{(9)}^0}{RT}\right) = \frac{X_{\text{CO}_2}}{X_{\text{CO}}} \frac{1}{(f_{\text{O}_2})^{1/2}}, \quad (11)$$

where R is the universal gas constant ($8.314 \text{ J K}^{-1} \text{ mol}^{-1}$), X_i is the mole fraction of species i , and $\Delta_r G_{(8)}^0$ and $\Delta_r G_{(9)}^0$ are the Gibbs free energies of reaction in J mol^{-1} for (8) and (9) respectively—functions of temperature given in Ortenzi et al. (2020), based on Fegley (2013). Equations (10) and (11) assume surface pressure $p_{\text{surf}} = 1 \text{ bar}$, whilst T is taken to be the temperature the melt would have once it has risen adiabatically to the surface:

$$T(p = p_{\text{surf}}) = T_{\text{melt}}(p_{\text{melt}}) \cdot \exp\left[-\frac{\alpha_{\text{melt}}}{\rho_{\text{melt}} C_{p,\text{melt}}}(p_{\text{melt}} - p)\right], \quad (12)$$

where $C_{p,\text{melt}}$ is the heat capacity of the melt in $\text{J kg}^{-1} \text{ K}^{-1}$, α_{melt} is the thermal expansion coefficient in K^{-1} , ρ_{melt} is the density in kg m^{-3} , and T_{melt} and p_{melt} are the local temperature in K and pressure in Pa of the melt source. Values for the thermodynamic parameters are listed in Table 1.

From the model outlined above, we can calculate the outgassed mass M_i in kg of each volatile species i at a given time, accumulated over all previous time steps and over all cells in the domain:

$$\begin{aligned} M_{\text{H}_2\text{O}}^{\text{atm}} &= \chi_{\text{extr}} \sum_{j=1}^{\text{times cells}} \sum_{k=1}^{\text{cells}} \chi_{\text{H}_2\text{O},j,k}^{\text{melt}} F_{j,k} V_k \frac{X_{\text{H}_2\text{O}}}{X_{\text{H}_2} + X_{\text{H}_2\text{O}}} \rho_{\text{mtl}} \\ M_{\text{H}_2}^{\text{atm}} &= \chi_{\text{extr}} \sum_{j=1}^{\text{times cells}} \sum_{k=1}^{\text{cells}} \chi_{\text{H}_2\text{O},j,k}^{\text{melt}} F_{j,k} V_k \frac{X_{\text{H}_2}}{X_{\text{H}_2} + X_{\text{H}_2\text{O}}} \frac{m_{\text{H}_2}}{m_{\text{H}_2\text{O}}} \rho_{\text{mtl}} \\ M_{\text{CO}_2}^{\text{atm}} &= \chi_{\text{extr}} \sum_{j=1}^{\text{times cells}} \sum_{k=1}^{\text{cells}} \chi_{\text{CO}_2,j,k}^{\text{melt}} F_{j,k} V_k \frac{X_{\text{CO}_2}}{X_{\text{CO}} + X_{\text{CO}_2}} \rho_{\text{mtl}} \\ M_{\text{CO}}^{\text{atm}} &= \chi_{\text{extr}} \sum_{j=1}^{\text{times cells}} \sum_{k=1}^{\text{cells}} \chi_{\text{CO}_2,j,k}^{\text{melt}} F_{j,k} V_k \frac{X_{\text{CO}}}{X_{\text{CO}} + X_{\text{CO}_2}} \frac{m_{\text{CO}}}{m_{\text{CO}_2}} \rho_{\text{mtl}}, \end{aligned} \quad (13)$$

where χ_{extr} is the percentage of volcanism that is extrusive, $F_{j,k}$ is the local melt fraction in a cell, V_k is the volume of that cell in m^3 , m_i is molar mass of species i in kg mol^{-1} , and ρ_{mtl} is the local density of the solid mantle in kg m^{-3} . Note that χ has units of weight fraction and X has units of mole fraction. The melt volumes correspond to a 2D annulus, later scaled up to 3D by a dimensionalisation factor.

The partial pressure in Pa outgassed to the atmosphere for species i is:

$$p_i = \frac{M_{\text{tot}} X_{i,\text{tot}} g}{4\pi R_E^2}, \quad (14)$$

where M_{tot} is the sum over species of the outgassed masses from equation (13) in kg, $X_{i,\text{tot}}$ is the species' mole fraction, g is the acceleration due to gravity at the surface (9.8 ms^{-2}), and R_E is the radius of Earth (6371 km). We assume that the gas reaches the atmosphere instantaneously.

2.5. Initial conditions and free parameters

The main study involves >700 cases with random values for eight free input parameters (Table 2), identified as the main unknown parameters potentially affecting the early Earth evolution. Input values for each case are drawn from uniform distributions, with one exception. This section outlines the choice of bounds.

Table 2: Input parameters varied in this study. Values are drawn from random uniform distributions bounded by the values in the Range column, with the exception of T_{ini} (see text).

SYMBOL	DESCRIPTION	RANGE	UNITS
$\log(f_{\text{O}_2}) - \text{IW}$	Mantle redox shift from IW	[-3, 4]	dex
$\chi_{\text{H}_2\text{O}}^{\text{ini}}$	Initial mantle H ₂ O content	[50, 450]	wt. ppm
$\chi_{\text{CO}_2}^{\text{ini}}$	Initial mantle CO ₂ content	[22, 180]	wt. ppm
T_{surf}	Temperature at surface	[273, 333]	K
T_{ini}	Initial temperature at top of convecting layer	[1750, 2000]	K
D_{lid}	Initial lid thickness	[10, 43]	km
ΔT_c	Initial core temperature jump	[0, 1750]	K
χ_{extr}	Extrusive volcanism percentage	[10, 40]	wt. %

2.5.1. Choice of initial temperatures

The initial mantle temperature profile is set by four unknown parameters: planet surface temperature, T_{surf} , initial stagnant lid thickness, D_{lid} , initial temperature at the base of the lithosphere, T_{ini} , and core temperature jump, ΔT_c . Temperatures increase linearly from T_{surf} to T_{ini} , and then follow an initially adiabatic profile from below the upper thermal boundary layer to the core-mantle boundary. The temperature contrast between the base of the mantle and the core is fixed at ΔT_c . We enforce an initial temperature cut-off at the solidus.

Although evidence of surface temperatures covering our age of interest is scant, oxygen isotope ratios from the 4.4 Ga Jack Hills zircons imply a surface temperature enough to host liquid oceans (Valley et al., 2002). Thus we allow T_{surf} to vary from 0 to 60°C. Our constant T_{surf} is an approximation; in reality this value varies spatially and is linked to outgassing via greenhouse warming.

The temperatures in Earth’s mantle after the last magma ocean stage are unknown. We adopt a range of 1750–2000 K in T_{ini} . This study’s effective distribution of T_{ini} is not uniform because higher values of T_{ini} were more likely to result in numerical instabilities. Values of $T_{\text{ini}} > 2000$ K always led to numerical errors. However, temperatures do increase beyond this initial value due to radiogenic heating. Archean komatiite records suggest an upper mantle potential temperature of at most ~ 1970 K (Herzberg et al., 2010), corresponding to upper mantle temperatures comparable with those investigated here (our T_{ini} values refer to the actual temperatures below an initial upper thermal boundary layer, hence the potential temperatures would be slightly smaller).

The initial adiabatic profile implies an already-convecting mantle. However, at the onset of our simulations, the mantle is gravitationally stable. Hence we slightly perturb the temperature field to trigger convection. Initial temperatures are close to the solidus, so melting and outgassing begin quickly. Regardless, this temperature profile quickly starts evolving, and its initial shape is not significant to the results. The stagnant lid thickness also adjusts according to the temperature profile. Very thick lithospheres (~ 100 km) would inhibit melt production to the extent that no outgassing would occur within 700 Myr.

2.5.2. Choice of initial volatile contents

Most of the bulk Earth’s accreted volatile content may have been expelled during magma ocean degassing. The crystallised mantle’s initial H₂O and CO₂ contents, $\chi_{\text{H}_2\text{O}}^{\text{ini}}$ and $\chi_{\text{CO}_2}^{\text{ini}}$ in weight percent, are the amounts of volatiles remaining after degassing adopted from the magma ocean model of Elkins-Tanton (2008). The most water-rich scenario would correspond to just below an Earth ocean mass. These estimates are consistent with more recent modelling work by Barth et al. (0). Hier-Majumder and Hirschmann (2017) found comparable but slightly elevated values considering faster freezing of the magma ocean. Elkins-Tanton (2008) considers primordially-accreted volatile contents of 0.05–0.5 weight percent H₂O and 0.01–0.1 weight percent CO₂, although the true values are poorly constrained.

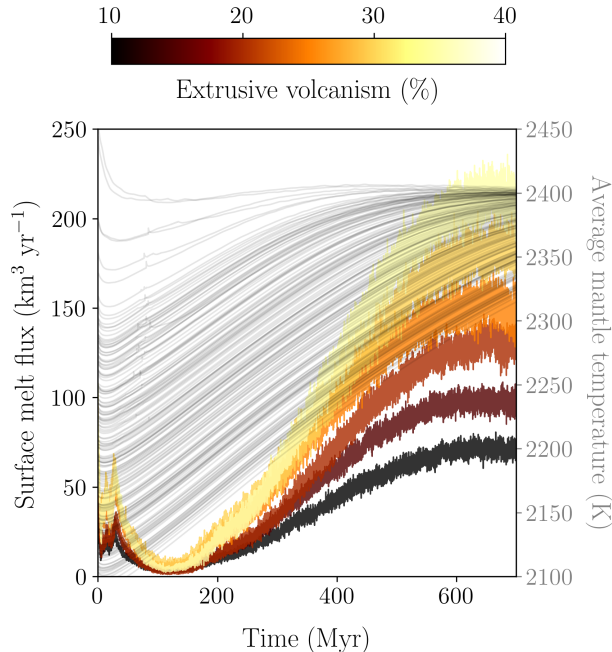


Figure 1: The evolution of the extrusive volumetric melt production rate, assuming a melt density of 3000 kg m^{-3} . Note that these values represent only 10–40% of the total melt production. Cases are binned to 5%-increments in the extrusive volcanism fraction, and averaged over all other input parameters (Table 2). Lighter colours indicate higher extrusive volcanism fractions. Overlain in solid grey lines and corresponding to the secondary y -axis are the evolutions of the mean temperature over the whole mantle, for each individual model run.

2.5.3. Choice of mantle oxidation states

Geochemical clues mostly agree that since around 3.8 Ga or earlier, the Archean upper mantle was about as oxidised as present (Canil, 1997; Delano, 2001; Trail et al., 2011; Nicklas et al., 2018; Armstrong et al., 2019), although other analyses suggest a more gradual oxidation up to QFM (Aulbach and Stagno, 2016; Nicklas et al., 2019). Trail et al. (2011) investigated Hadean zircons with ages between 4.0–4.36 Ga and derived an oxidation state around QFM. If these zircons did indeed come from primitive mantle melts as suggested by Trail et al. (2011), this would suggest an oxidised mantle almost directly after the Moon-forming impact.

We allow mantle f_{O_2} to vary between the minimum Hadean value of three log-units below the equilibrium with the IW buffer (Wood et al., 2006), and a typical modern value of four log-units above the equilibrium. We assume a constant oxidation state, and later test the effect of $\log(f_{\text{O}_2})$ increasing linearly.

2.5.4. Choice of extrusive volcanism percentages

Only a fraction of magma will rise high enough to extrude and outgas at the surface. The remaining melt in the intrusive component will eventually replenish the mantle. Crisp (1984) estimate an extrusive volcanism percentage of 6–25% for intracontinental and island arc settings, and 16–33% at mid-ocean ridges and hotspots. Because this value is unknown for early Earth, we allow it to vary between 10% and 40% (Grott et al., 2011). We do not consider any diffuse degassing from intrusive volcanism, although fluid pressure would indeed transport intrusive magmatic gas to the surface through rock fissures.

3. Results

Before speciation, the total C (or H) outgassing flux is proportional to the product of the C (or H) melt concentration and the extrusive melt production rate. In principle, either of these factors has the

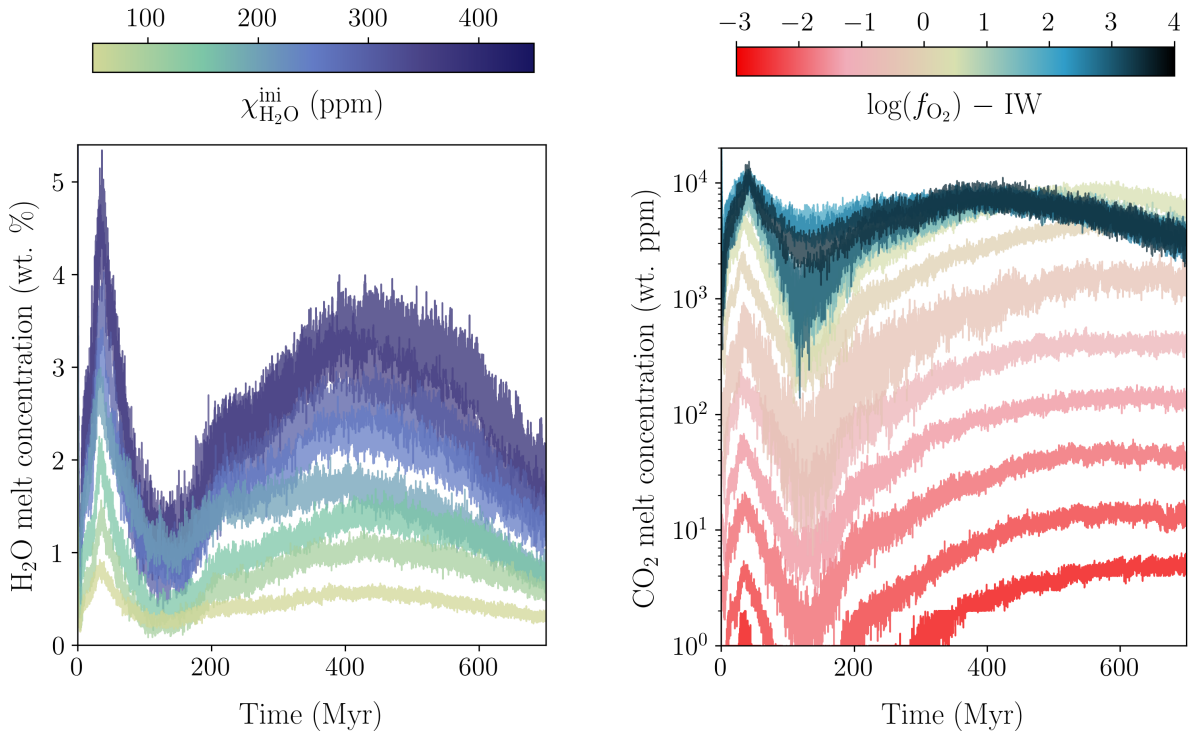


Figure 2: The evolution of melt volatile contents for H₂O (*left*; in weight percent) and CO₂ (*right*; in weight ppm). Cases are binned according to their values of the main input parameter controlling melt partitioning (see text): for H₂O this is the initial mantle H₂O content ($\chi_{\text{H}_2\text{O}}^{\text{ini}}$), and for CO₂ this is the mantle oxygen fugacity (f_{O_2}) with respect to the iron-wüstite buffer (IW). Lines are coloured by bin and show the mean melt concentration per time interval, given random values for the other input parameters.

potential to scale outgassing dramatically, although they do not necessarily show the same variance. We will first present the melt production rates and melt concentrations from the model. Then we will describe the resulting outgassing fluxes, their final speciation modulated by f_{O_2} .

3.1. Thermal history and melt production

The thermal histories underlying the outgassing model are shown in figure 1. Mean mantle temperatures gradually increase due to powerful primordial radiogenic heating and relatively sluggish stagnant lid convection. The temperature dependence of viscosity acts as a thermostat, such that by 700 Myr, average mantle temperatures converge to $\sim 2320\text{--}2400$ K.

The first ~ 50 Myr see spikes in the melt flux. Directly after magma ocean solidification, the mantle temperature is still very close to the solidus. In these conditions, slight mass movement from convection can trigger immediate re-melting. This depletes the residual mantle and raises the solidus temperature. Melting is revived once either radiogenic heating warms the upper mantle, or convection upwells undepleted material from the lower mantle to pressures of ≤ 12 GPa.

Note that higher initial temperatures than considered here would lead to unphysical conditions, with most of the mantle above the solidus temperature. Whilst a much wetter mantle might aid melting, we do not find a dramatic effect of $\chi_{\text{H}_2\text{O}}^{\text{ini}}$ on the overall melt production. We do not include dehydration's stiffening effect on viscosity.

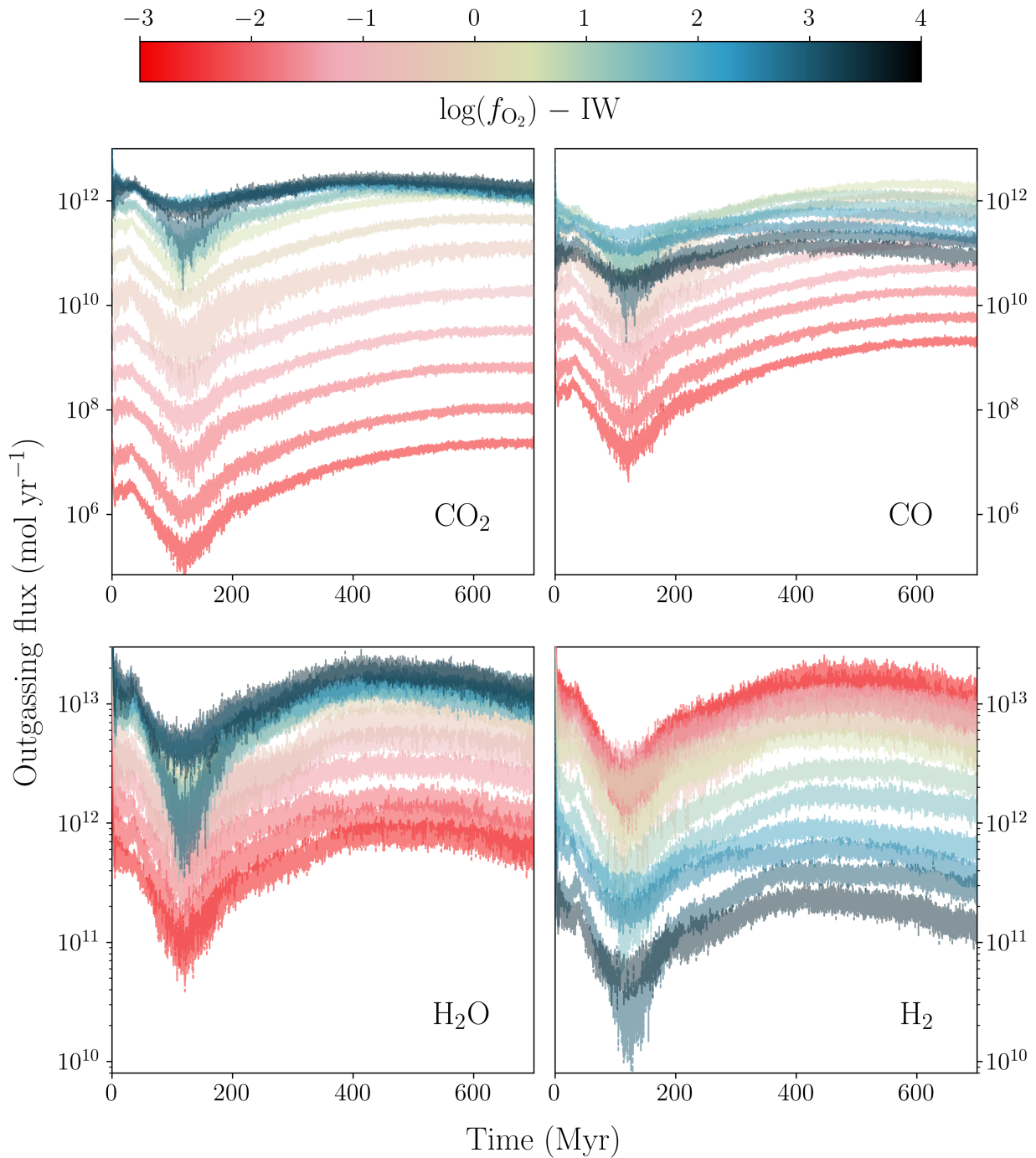


Figure 3: The mean evolution of volcanic outgassing fluxes for CO_2 (top left), CO (top right), H_2O (bottom left), and H_2 (bottom right). Coloured lines from red to dark blue indicate increasingly oxidised mantles, binned to increments of 0.5 log-units in mantle oxygen fugacity (f_{O_2}) with respect to the iron-wüstite buffer (IW), and averaged across all other input parameters.

3.2. Melt contents of H₂O and CO₂

Due to the different chemistry controlling the partitioning of C and H₂O into the melt (section 2.3), $\chi_{\text{H}_2\text{O}}^{\text{melt}}$ and $\chi_{\text{CO}_2}^{\text{melt}}$ respond to different model parameters. These behaviours are reflected in figure 2. H₂O partitioning into the melt depends directly on the local mantle H₂O abundance, the maximum of which is set by $\chi_{\text{H}_2\text{O}}^{\text{ini}}$. The effect of mantle content on melt content is non-linear: in equation (7), $\chi_{\text{H}_2\text{O}}^{\text{melt}}$ depends on the local melt fraction, whilst the presence of water facilitates melting by suppressing the solidus.

Carbon partitioning, in contrast, is strongly redox-dependent. This is true for the regime we model, where graphite is the stable phase, but would not apply to more oxidising conditions (Stagno, 2019). Note, that the local mantle source CO₂ concentration can still limit $\chi_{\text{CO}_2}^{\text{melt}}$. This effect is most obvious at very low values of $\chi_{\text{CO}_2}^{\text{ini}}$ below 50 ppm, or for cases approaching maximum outgassing—in either situation the local carbon inventories can run out. The most carbon-rich simulations can be seen (figure 2) to reach peak $\chi_{\text{CO}_2}^{\text{melt}}$ before 700 Myr for this reason. Meanwhile, the effect of f_{O_2} on $\chi_{\text{CO}_2}^{\text{melt}}$ is drastic everywhere. With each step of one log-unit below the IW buffer, we see $\chi_{\text{CO}_2}^{\text{melt}}$ drop by an order of magnitude.

There is an early transient stage where the melt abundance drops steeply. This is associated with the early pulse of melting and hence depletion (figure 1).

3.3. Exploration of outgassing scenarios

A notable result of this work is that all scenarios, regardless of oxidation state, produce outgassing no higher than total estimates for modern Earth (e.g., Catling and Kasting, 2017). To see why this is, here we examine what controls outgassing rates in this model.

3.3.1. Outgassing as a function of mantle oxidation state

As expected (Holland, 1984; Kasting et al., 1993), there is a heavy dependence of the outgassing rate on f_{O_2} . Figure 3 shows the evolution of each species’ mean outgassing flux in mol yr⁻¹, with cases binned by f_{O_2} and all other input parameters varying according to a random uniform distribution (Table 2). A more oxidised mantle is associated with more CO₂ and H₂O outgassing, and a more reduced mantle is associated with more H₂ outgassing. The pattern for CO is more complicated. It peaks around IW: low f_{O_2} limits the amount of total carbonate that can dissolve into the melt, despite the gas-phase equilibrium favouring CO over CO₂. Outgassing rates increase slightly with time (by 10–15%) during the 700 Myr modelled. The early pulse of outgassing is associated with the early pulse of melting (figure 1).

To illustrate the dependence of evolved outgassing on f_{O_2} , figure 4 shows every run’s cumulative outgassed mass per species, as a function f_{O_2} . Both C- and H-bearing species are well-separated in terms of mass, except for cases close to the IW buffer. Increasing f_{O_2} from IW - 3 to IW + 4 is associated with an increase of over an order of magnitude in the mass of H₂O, and an increase of at least five orders of magnitude for CO₂, whilst the mass of H₂ decreases. The hydrogen speciation shows a gradient in redox. The carbon speciation also shows a gradient in redox, whilst the total amount of carbon depends on partitioning (itself a function of redox).

It is worth emphasising that figure 4 does not show the actual gas masses residing in the atmosphere. For instance, the atmospheric partial pressure of H₂O is limited to the saturation vapour pressure of liquid water; on the Myr-timescales of this model, the cooling timescale of the outgassed plume to ambient atmospheric temperatures is irrelevant. At $T_{\text{surf}} = 333$ K, the saturation vapour pressure is 0.2 bar. The cumulative mass of H₂O (which would quickly condense) is at most about a tenth of modern Earth’s ocean mass, which would support the idea that earlier magma ocean degassing supplied a significant fraction of the original ocean mass (Pahlevan et al., 2019).

The influence of f_{O_2} on the outgassed volatile masses is built into the model. Intrinsically, there are three reasons for the mass dependence in figure 4. The first two reasons comprise the redox-dependent speciation (setting total carbon) and volatile speciation (setting $[\text{H}_2\text{O}]/[\text{H}_2]$ and $[\text{CO}_2]/[\text{CO}]$) already described. The third reason is that the reduced gases investigated here have a lower molecular mass than their oxidised counterparts. Thus, for equal quantities outgassed, reduced atmospheres are necessarily less massive than oxidised atmospheres.

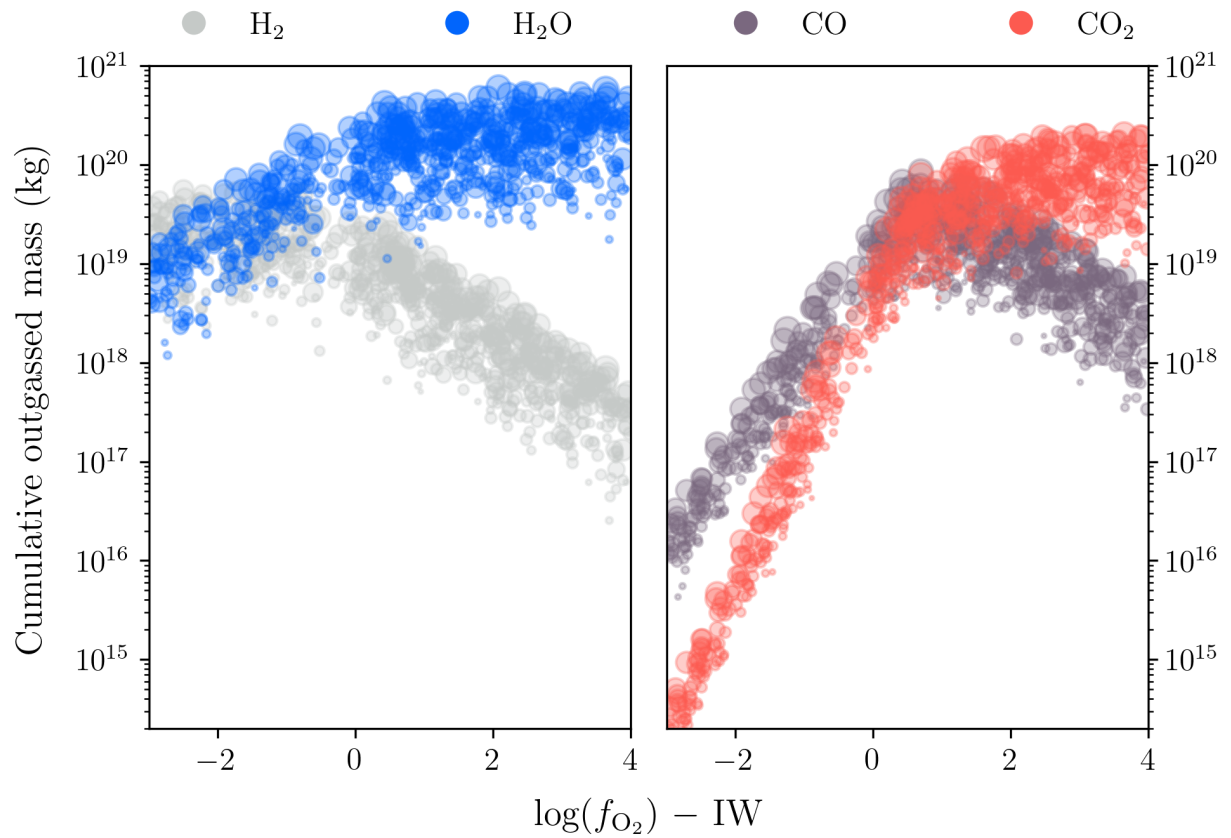


Figure 4: Each simulation's final cumulative outgassed masses of H_2 (grey dots), H_2O (blue dots), CO (aubergine dots), and CO_2 (coral dots), as a function of the mantle oxygen fugacity (f_{O_2}) with respect to the iron-wüstite buffer (IW). Marker size increases with higher cumulative melt volume. All 762 parameter combinations are shown.

Table 3: Final partial pressures, masses, and fluxes for each species after 700 Myr of outgassing, binned by mantle oxygen fugacity (f_{O_2}) with respect to the iron-wüstite buffer (IW). Fluxes represent averages over the last 10 Myr. Results are shown as the bin medians, with 1σ limits super- and subscripted.

		$\log(f_{\text{O}_2}) - \text{IW}$						
		[-3, -2)	[-2, -1)	[-1, 0)	[0, 1)	[1, 2)	[2, 3)	[3, 4]
FINAL PRESSURE bar	CO ₂	0.0 ^{+0.0} _{-0.0}	0.0 ^{+0.0} _{-0.0}	0.0 ^{+0.1} _{-0.0}	1.2 ^{+1.4} _{-0.8}	3.5 ^{+3.1} _{-1.8}	5.9 ^{+6.3} _{-3.3}	7.2 ^{+6.8} _{-4.5}
	CO	0.0 ^{+0.0} _{-0.0}	0.0 ^{+0.0} _{-0.0}	0.1 ^{+0.3} _{-0.1}	2.1 ^{+2.3} _{-1.3}	2.4 ^{+2.3} _{-1.4}	1.2 ^{+1.3} _{-0.6}	0.5 ^{+0.6} _{-0.3}
	H ₂ O	0.3 ^{+0.3} _{-0.2}	1.3 ^{+1.6} _{-0.7}	5.1 ^{+7.0} _{-2.7}	21.3 ^{+18.7} _{-11.7}	32.2 ^{+26.2} _{-17.0}	38.5 ^{+34.0} _{-20.3}	51.0 ^{+31.4} _{-30.6}
	H ₂	5.7 ^{+4.2} _{-3.5}	6.4 ^{+7.1} _{-3.0}	8.9 ^{+10.0} _{-3.8}	10.0 ^{+7.9} _{-5.2}	5.2 ^{+3.7} _{-2.8}	2.0 ^{+2.0} _{-1.1}	0.8 ^{+0.5} _{-0.6}
FINAL MASS kg ($\times 10^{18}$)	CO ₂	0.0 ^{+0.0} _{-0.0}	0.0 ^{+0.1} _{-0.0}	0.5 ^{+1.3} _{-0.3}	15.3 ^{+19.0} _{-9.6}	40.7 ^{+30.2} _{-21.5}	59.6 ^{+52.0} _{-29.9}	66.7 ^{+72.1} _{-38.2}
	CO	0.0 ^{+0.0} _{-0.0}	0.3 ^{+0.5} _{-0.2}	2.2 ^{+3.9} _{-1.2}	19.0 ^{+20.6} _{-10.9}	16.1 ^{+15.7} _{-8.3}	7.5 ^{+10.0} _{-3.5}	3.1 ^{+3.8} _{-1.9}
	H ₂ O	9.4 ^{+7.8} _{-5.5}	23.9 ^{+27.1} _{-11.9}	57.9 ^{+60.4} _{-27.1}	128.7 ^{+106.6} _{-74.1}	154.9 ^{+129.0} _{-93.6}	171.7 ^{+153.2} _{-102.4}	220.2 ^{+137.2} _{-142.1}
	H ₂	18.2 ^{+18.2} _{-10.4}	13.3 ^{+14.3} _{-6.2}	12.2 ^{+10.5} _{-6.2}	6.8 ^{+5.7} _{-3.7}	2.8 ^{+2.3} _{-1.7}	1.0 ^{+0.9} _{-0.6}	0.4 ^{+0.3} _{-0.2}
FINAL FLUX mol yr ⁻¹ ($\times 10^{12}$)	CO ₂	0.0 ^{+0.0} _{-0.0}	0.0 ^{+0.0} _{-0.0}	0.0 ^{+0.1} _{-0.0}	0.7 ^{+1.2} _{-0.4}	1.3 ^{+1.4} _{-0.8}	1.4 ^{+1.6} _{-0.8}	1.8 ^{+2.3} _{-1.2}
	CO	0.0 ^{+0.0} _{-0.0}	0.0 ^{+0.0} _{-0.0}	0.2 ^{+0.4} _{-0.1}	1.5 ^{+1.8} _{-0.8}	0.9 ^{+1.1} _{-0.5}	0.3 ^{+0.5} _{-0.2}	0.1 ^{+0.2} _{-0.1}
	H ₂ O	0.8 ^{+0.9} _{-0.6}	1.9 ^{+1.8} _{-1.2}	4.6 ^{+4.2} _{-2.6}	9.1 ^{+8.6} _{-5.4}	11.4 ^{+13.1} _{-6.5}	11.3 ^{+10.7} _{-7.8}	14.3 ^{+15.9} _{-7.4}
	H ₂	12.9 ^{+15.0} _{-8.1}	8.7 ^{+7.6} _{-4.8}	8.2 ^{+7.4} _{-5.0}	4.3 ^{+3.7} _{-2.6}	1.8 ^{+2.4} _{-1.1}	0.5 ^{+0.8} _{-0.3}	0.2 ^{+0.3} _{-0.1}

3.3.2. Other factors influencing outgassing

Figure 6 summarises the Spearman’s rank (nonlinear) correlation coefficients between each species’ outgassing flux, averaged over the final 10 Myr, and the eight input parameters plus the melt volumes and volatile concentrations. This section explains how the remaining correlations stem from the model.

Influence of initial temperatures. We find virtually no correlation between initial temperature conditions and outgassing fluxes after 700 Myr of convection. However, an initially hotter mantle closer to the solidus temperature forces a sharp pulse of melting in the first 100 Myr, expelling massive amounts of water and indeed raising the total mass of water outgassed. This is also not to say that instantaneous local temperatures are unimportant, as they affect the melt fraction as well as the equilibrium constants in (3), (10), and (11).

Influence of extrusive volcanism fractions. From (13), we expect an approximately linear relationship between the maximum outgassing flux and the fraction of melt allowed to contribute to outgassing. Although the correlation between this fraction and the computed outgassing fluxes is not as strong as f_{O_2} , accounting for extrusive volcanism in this model automatically downscales outgassing. For example, all else being equal, the difference between $\chi_{\text{extr}} = 10\%$ and $\chi_{\text{extr}} = 100\%$ would be an order of magnitude in outgassing.

Role of melt production rate versus melt volatile content. Figure 6 also shows the correlations of all outgassing fluxes with the instantaneous volatile melt concentrations and melt production rates. CO₂ outgassing fluxes correlate more strongly with CO₂ melt concentrations than with the total melt production rates, whilst the opposite appears to be true for H₂O. Note that H₂O melt concentrations are not independent of melt volumes because of partitioning of water into the melt—H₂O concentrations are largest for the smallest melt fractions. To some degree, the relative strengths of the correlations reflect the experimental variances in melt production and volatile melt contents, given the ranges of the prior distributions on the input parameters. Nevertheless, in our simulations, outgassing will be ultimately limited by the volatile budget of the mantle. Thus rates of outgassing would not scale indefinitely with rates of volcanism.

3.3.3. Redox-marginalised outgassing distributions

Figure 5 presents the experimental distributions of each species’ cumulative outgassed partial pressures, shown for different redox bins. Again, the dominant effect of f_{O_2} is visible in how these distributions are separated along the x -axis. The median and 1σ values of these partial pressures are quantified in Table 3, along with the corresponding masses and fluxes.

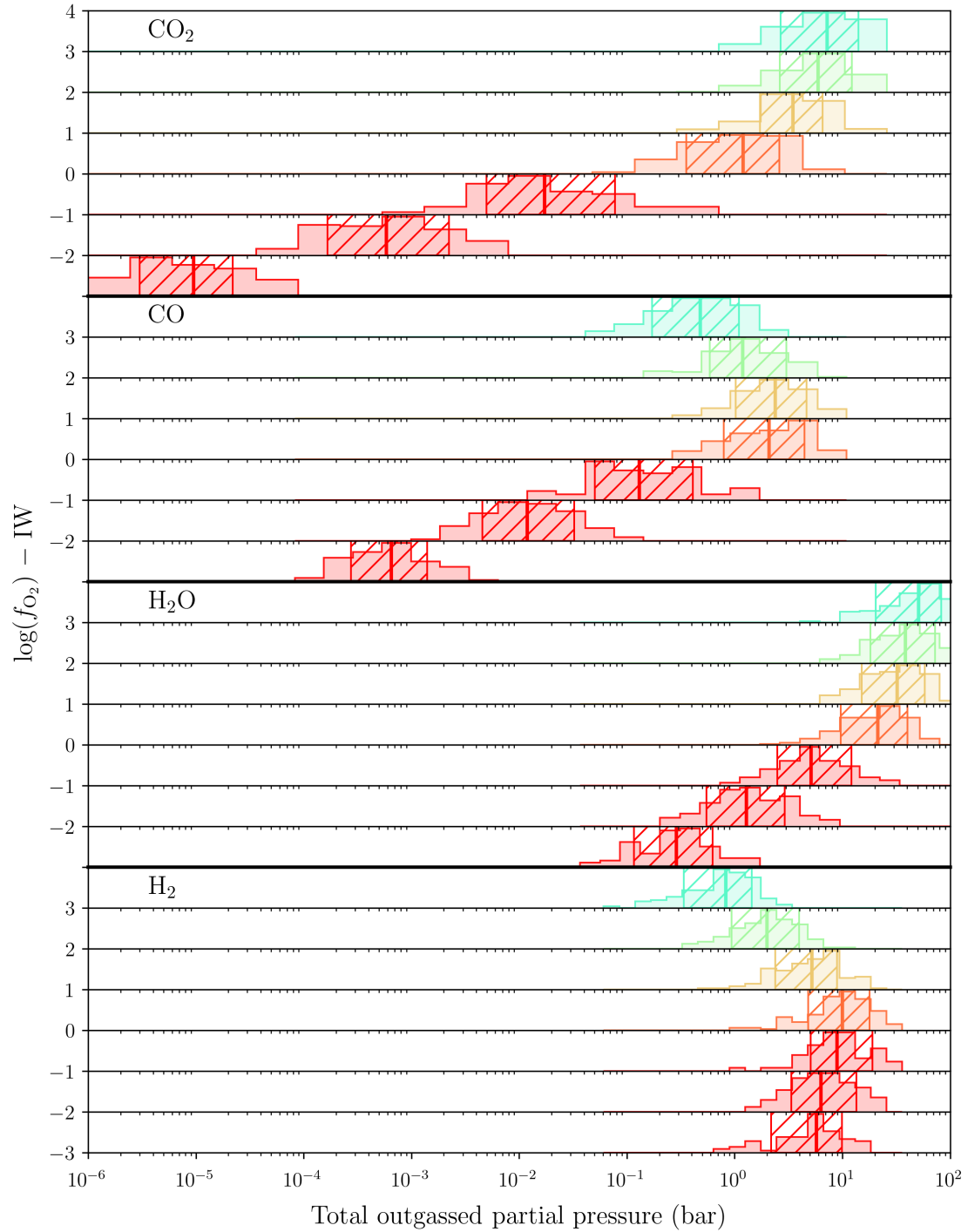


Figure 5: Histograms of the empirical distribution of 700-Myr-cumulative outgassed masses for (from top to bottom) CO₂, CO, H₂O, and H₂. Distributions are marginalised across the mantle oxygen fugacity (*f*_{O₂}) with respect to the iron-wüstite buffer (IW), where each colour shows one of five log(*f*_{O₂}) bins as indicated by the *y*-axis ticks. Bold vertical lines indicate the medians; hatched regions mark the 1σ width.

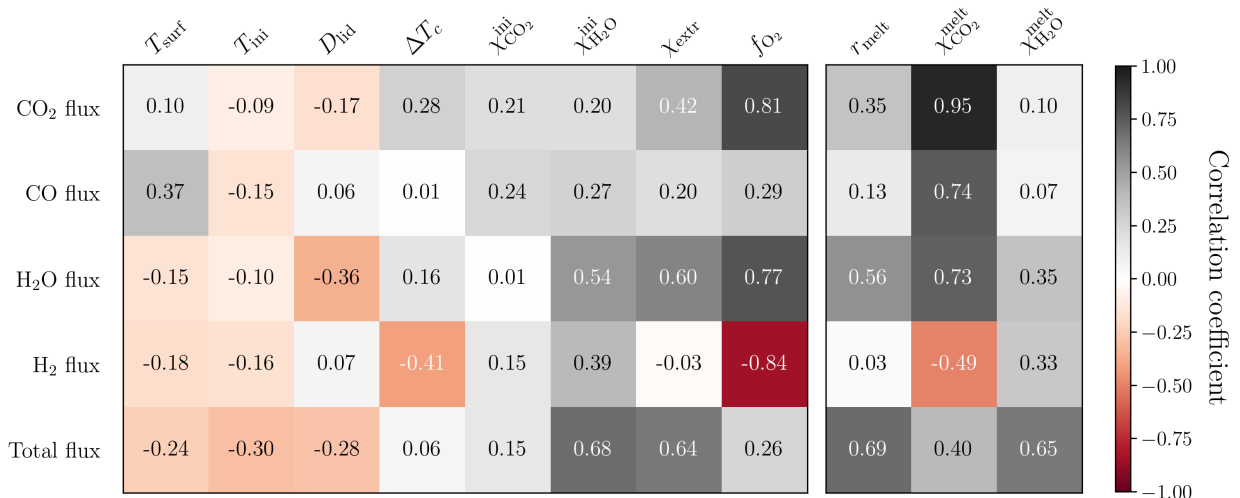


Figure 6: (Left): The matrix of Spearman’s rank correlation coefficients between input parameters and outgassing fluxes averaged over the final 10 Myr, plus the summed flux of all outgassed molecules for the same time frame. Symbols are defined in Table 2. (Right): The same, but for key intermediate output variables—the volumetric melt production rate, τ_{melt} , and the melt concentrations of CO₂ and H₂O, $\chi_{\text{CO}_2}^{\text{melt}}$ and $\chi_{\text{H}_2\text{O}}^{\text{melt}}$. Note that the moderate correlation between $\chi_{\text{CO}_2}^{\text{melt}}$ and H-species outgassing is due to the mutual effect of f_{O_2} on both quantities, while the correlation of f_{O_2} with the total flux appears low because it does not affect the sum of H₂ and H₂O.

3.4. Secular mantle oxidation

Several mechanisms for mantle oxidation have been proposed (e.g., Wood et al., 2006; Sharp et al., 2013; Gaillard and Scaillet, 2014; Wordsworth et al., 2018; Schaefer and Elkins-Tanton, 2018; Nicklas et al., 2019), including degassing itself (Kasting et al., 1993). These mechanisms would be associated with different durations. By tracking the concentration of abundant multivalent cations, one might self-consistently evolve the mantle redox state within our outgassing scenarios. We leave this to future work, and as a first step, simply consider a linear increase of $\log(f_{\text{O}_2})$ from IW -2 to IW $+2$ over 700 Myr, for a new set of 110 runs with otherwise random parameters as before (Table 2).

Figure 7 demonstrates that secularly increasing $\log(f_{\text{O}_2})$ results in cumulative outgassing not obviously distinguishable from a constant $\log(f_{\text{O}_2}) - \text{IW} \in [0, 2]$. The spread in these cases would be largely explained by variations in the melting rate.

Low f_{O_2} does not affect melt concentrations of H-species, such that the same total amount of total H can be outgassed. Carbon, meanwhile, is strongly limited in melts during the early reduced stage, which might imply lower cumulative partial pressures. However, Figure 7 suggests that this effect is somewhat muted due to the scatter induced by other unknown parameters. Note, regardless, that small differences in cumulative outgassing could represent dramatic differences in the ultimate atmospheric composition; scenarios of evolving mantle redox likely deserve more rigorous treatment than attempted here.

4. Discussion

4.1. Some important considerations about the assumptions in this model

4.1.1. Viscosity treatment

This work has considered a single set of upper mantle rheological parameters, corresponding to the canonical Arrhenius viscosity law for wet olivine from Karato and Wu (1993). Lower mantle rheology is taken from Tackley et al. (2013). Different viscosity treatments could potentially influence melting rates and therefore outgassing rates.

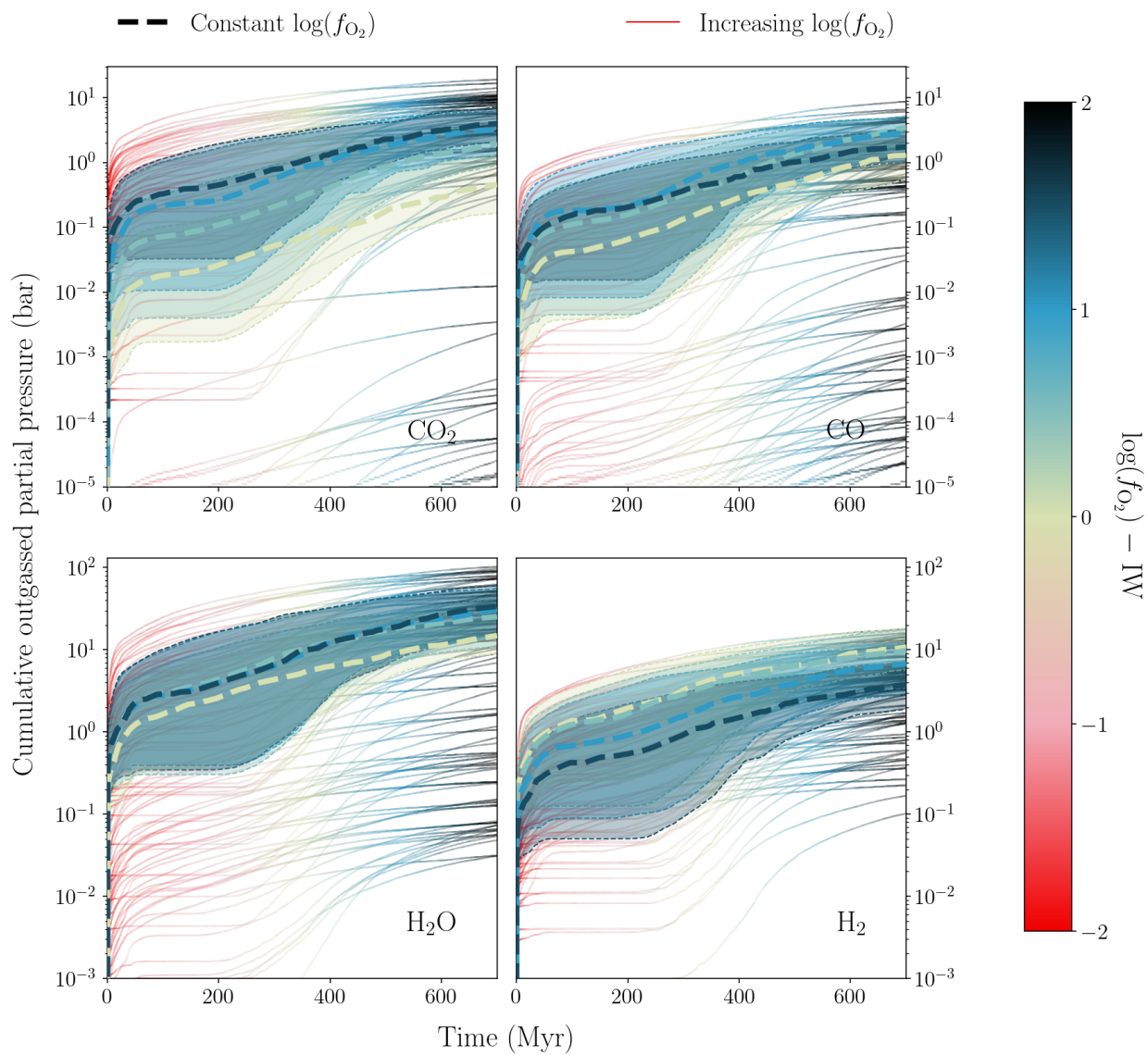


Figure 7: The evolution of the cumulative outgassed partial pressure for scenarios where the mantle oxygen fugacity (f_{O_2}) with respect to the iron-wüstite buffer (IW) increases log-linearly from IW $- 2$ to IW $+ 2$ over 700 Myr (thin solid gradient lines; $N = 110$). For comparison, also shown are the f_{O_2} -bin medians of previous scenarios where f_{O_2} is fixed randomly between IW and IW $+ 2$ (thick dashed lines; $N = 147$), where the thin dashed lines spanned by swaths indicate 1σ above and below the median. Subplots show the species CO_2 (top left), CO (top right), H_2O (bottom left), and H_2 (bottom right). The colour indicates the instantaneous mantle redox.

However, several regulation mechanisms exist such that an immediate weakening of upper mantle viscosity, whilst increasing the convective velocity, may not lead to dramatically higher melting in the long term. Firstly, latent heat loss associated with any melting that does occur would cool the mantle (the latent heat of melting is indeed modelled here). These lowered temperatures would both limit further melting and stiffen the local viscosity in a negative feedback loop (Ogawa and Yanagisawa, 2011). Secondly, a sudden increase in convective velocity would lead to faster replenishment of depleted material in the upper mantle, which promotes melting; yet, thirdly, this effect would be offset simultaneously by more efficient cooling of the mantle, which suppresses melting.

The Karato and Wu (1993) law for wet diffusion creep does have a relatively weak temperature dependence and a strong pressure dependence, which could reduce some of the feedbacks described here. Nevertheless, as in Dorn et al. (2018), we expect that melting is ultimately controlled by the lower mantle viscosity because rapid flow in the upper mantle merely leads to rapid depletion. With that said, we would still emphasise that the results here are subject to our chosen viscosity treatment, and should be interpreted as such.

4.1.2. *Submarine versus subaerial outgassing*

We have assumed that all outgassing is subaerial and occurs at 1 bar. Several independent constraints place an upper limit on either the surface barometric pressure or $p\text{N}_2$ at 1.1 bar for 3.5–2.7 Ga (Marty et al., 2013; Catling and Zahnle, 2020). A lack of plate motion might allow volcanic eruptions to construct topography above sea level relatively quickly (e.g., Olympus Mons, a Martian shield volcano comparable to Germany in area). In this case, volatiles would degas freely from surface lavas at atmospheric pressure. Because near 1 bar there is almost no effect on gas solubility or f_{O_2} in our chosen parameterisations, we do not consider solubility or any redox change during degassing itself. If most outgassing occurred on the seafloor, then the higher pressures would allow melts to retain more volatiles, as long as the gas and melt are in equilibrium (e.g., eruptions are not explosive). Global outgassing rates would then be lower than predicted here, and show a different ratio of outgassing species (Gaillard et al., 2011).

4.1.3. *Note on CH_4 outgassing*

We neglect the outgassing of CH_4 entirely because its vapour phase is not stable at the pressure, temperature, and redox ranges we consider (Zhang and Duan, 2009; Wetzel et al., 2013; Ramirez et al., 2014). Some CH_4 fluid could be produced from a reduced source at high pressures up to 11 GPa (Scott et al., 2004). Although CH_4 can also be stable at surface pressures, melt temperatures would be too high for it to degas directly.

4.1.4. *Buoyancy limit of melting*

As in Noack et al. (2014, 2017), we have not considered the possibility of melting at depths greater than 12 GPa. This assumes that basaltic melt is not buoyant above this pressure because it is denser than olivine (Ohtani et al., 1995). However, Mosenfelder et al. (2009) have suggested that basaltic melt can nevertheless remain less dense than ringwoodite and wadsleite up to ~ 25 GPa. Therefore the actual density crossover pressure could be lower than modelled here (e.g., Beuchert and Schmeling, 2013). This could increase the volume of the mantle annulus in which melting can occur, possibly leading to enhanced outgassing if all buoyant melt at depth reaches the base of the lithosphere. However, it may be that no additional melting occurs at these depths, depending on how the local mantle temperatures compare to the (strongly pressure-dependent) melting temperature.

4.1.5. *Stagnant lid outgassing effects*

Some general consequences of imposing a stagnant lid regime are listed below. This compilation is by no means complete and would benefit from future work. Noack et al. (2014), Tosi et al. (2017), Foley and Smye (2018), and Gaillard et al. (2021) also discuss how tectonic regimes can affect outgassing rates. The arguments here could be tentatively supported by the observation that Venus currently appears less volcanically-active than Earth (Smrekar et al., 2010).

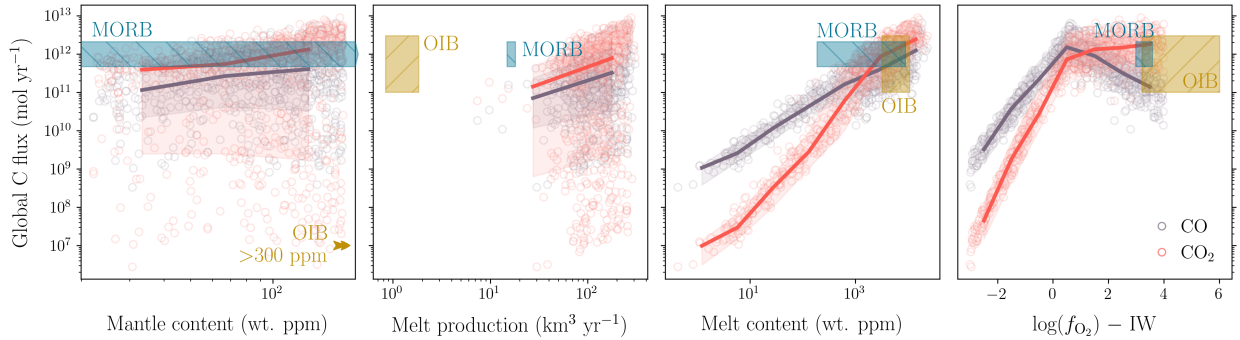


Figure 8: Summary of outgassing fluxes of CO (blue) and CO₂ (red), with respect to (from left to right) mantle source CO₂ content, melt production rate, melt CO₂ content, and mantle oxygen fugacity (f_{O_2}) relative to the iron-wüstite (IW) buffer. The mantle source concentrations in our model refer to the maximum (initial) values. All variables save f_{O_2} are represented by the final 10-Myr mean. Each hollow circle denotes an individual model run. Solid lines show the median of all runs, and swaths show the 1σ deviation. For context, we include estimates of modern Earth’s CO₂ outgassing, spanned by blue rectangles for the mid-ocean ridge (MOR) system, and by beige rectangles for hotspots. MOR estimates are taken from the data in Le Voyer et al. (2019) and Hauri et al. (2019), where the ranges of outgassing fluxes and melt production rates correspond to their quoted uncertainty on the global total, and the ranges of mantle and melt contents correspond to their log-normal sample distribution. For hotspots, the CO₂ flux lower limit is the sum from major hotspots from Hauri et al. (2019), and the generous upper limit is taken from Marty and Tolstikhin (1998); ocean island basalt (OIB) mantle source and melt concentrations are from Hauri et al. (2019); magma supply rates are the sum over 19 hotspots from Mjølde et al. (2010). Estimates of the mantle source f_{O_2} are from O’Neill et al. (2018) and Amundsen and Neumann (1992) for MORB and OIB respectively.

- i. *Interior temperatures:* For a constant mass, stagnant lid planets have hotter mantles because they lack the efficient cooling by subducting plates. This would enhance melting and volcanism.
- ii. *Melt volumes:* However, stagnant lid planets may be associated with less continuous melting *for the same interior temperature* because, three-fold, the melt zone is separated from the surface by a thick lithosphere, convection is weaker due to the lower temperature contrast, and the depleted mantle is not refertilised by subducting plates.
- iii. *Volatile inventories of the magma source:* Higher mantle volatile contents would lead to higher melt contents insofar as they reflect each other. The mantle source supplying stagnant lid volcanism should be less volatile-rich than the source of arc volcanism, which contains subducted crustal material relatively heavy in carbonates, organic carbon, and water (Wallace, 2005). The mid-ocean ridge source is drier, yet still generally appears carbon-rich compared to the initial concentrations we have adopted for the early degassed, differentiated mantle (Hauri et al., 2019). Hotspots, meanwhile, sample the deep mantle, which seems to contain both lingering nebular and recycled components (e.g., Miller et al., 2019). Analyses of ocean island basalts suggest even higher mantle source concentrations than mid-ocean ridges—likewise associated with high-CO₂ melts (e.g., Shorttle et al., 2015; Tucker et al., 2019; Broadley et al., 2019; Miller et al., 2019), as are ridge segments in proximity to hotspots (Le Voyer et al., 2019).
- iv. *Upper mantle hydration:* If subducted oceanic crust is wet, then the presence of water would depress the solidus (Katz et al., 2003). This could facilitate melting near subduction zones in a plate tectonics regime.

4.2. Observational context

4.2.1. Modern Earth’s volcanic outgassing

A key result from this work is that our stagnant lid outgassing model produces average outgassing rates no higher than those estimated for modern Earth under plate tectonics. Whereas $\sim 68\%$ of our cases more oxidised than IW + 3 have a CO₂ flux of between 0.6 and 4.1 Tmol yr⁻¹, estimates for Earth’s global CO₂ outgassing now rest at around 8.5 ± 2 Tmol yr⁻¹ (Catling and Kasting, 2017). Metamorphic degassing

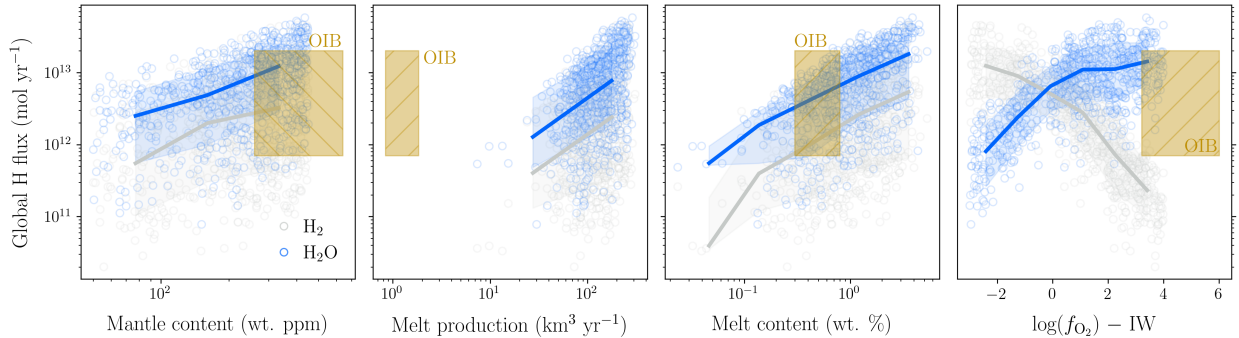


Figure 9: Analogous to Figure 8, but for H-bearing species, with H₂ flux in grey and H₂O flux in blue. The beige rectangle spans the estimate from Dasgupta and Hirschmann (2010) for CO₂ hotspot volcanism, multiplied by 7–8, the typical ratio of H₂O to CO₂ in hotspot volcanic gas from Holland (1984); i.e., following Catling and Kasting (2017). Mantle source concentrations refer to Hawaii estimates from Wallace (1998); melt concentrations are also Hawaii estimates from Wallace and Anderson (1998). Mid-ocean ridge volcanism is omitted because it is known to be very dry, compared to the range shown here. Other data are explained in the caption to figure 8.

and arc volcanism, irrelevant to a stagnant lid regime, both account for a quarter of this global estimate. Although our model does not necessarily apply to hotspot or mid-ocean ridge outgassing in a plate tectonics regime either, estimates of the modern rates of these processes might provide a useful point of context for illustrating the mechanisms that keep our outgassing results relatively low.

Namely, we see four main factors potentially influencing outgassing: mantle volatile content, melt production rates, melt volatile contents, and mantle oxidation state. To this end, figures 8 and 9 summarise our modelled outgassing rates as a function of these four factors, overplotted by the relevant present-day estimates for hotspot and ridge volcanism.

It should be noted upfront that our model may not be able to correctly capture modern ridge and hotspot outgassing rates, especially for CO₂. As explained in section 4.1.5 above, these processes sample recycled material generally having both (i) higher oxidation states, at the QFM buffer or above (Amundsen and Neumann, 1992; Moussallam et al., 2016; O’Neill et al., 2018; Moussallam et al., 2019), to which our carbon partitioning model does not apply, and (ii) higher source volatile concentrations than our quasi-primordial bulk mantle values (Hauri et al., 2019). The combined effect of (i) and (ii) is that CO₂ can potentially reach much higher melt concentrations on average. In oxidised conditions where carbonate is stable, abundant carbon would be lost very efficiently during partial melting.

Further to this point, modern outgassing rates are quite difficult to measure. Most quoted outgassing rates come from multiplying estimates of the melting rate with estimates of the concentration of volatiles in the melt. The volatile contents of melts are largely uncertain because melts are partially degassed; estimates rely on the behaviour of geochemical proxies (see Michael and Graham, 2015). An in-depth review of Earth’s ridge and hotspot outgassing rates is well beyond the scope of this work.

Mantle oxidation state. Whilst shown here for completeness, mantle f_{O_2} does not play an important role in controlling modern CO₂ or H₂O outgassing because the modern upper mantle is oxidised essentially everywhere, such that H₂ and CO would never be favoured, and carbon partitioning in the melt is not redox-dependent.

Melt production. Estimates of globally-integrated magma supply rates at mid-ocean ridges tend to show better agreement—most not far from 20 km³ yr⁻¹ (Crisp, 1984; Mjelde et al., 2010; Le Voyer et al., 2019)—although these estimates refer to the volume of all melt contributing to crust production, which may not necessarily be the same as the volume of melt contributing to outgassing. This study has found stagnant lid extrusive melting rates up to tenfold higher. Therefore melting rates alone would not explain our model’s low outgassing fluxes. Hotspots are more geographically sparse, and their global magma supply rate is lower than ridges.

Mantle concentrations. The ridge mantle source shows orders-of-magnitude variation in CO₂ concentrations (as derived from melt concentrations). This variation, extending from a minimum of 10 ppm to a maximum of 1980 ppm (Hauri et al., 2019), encompasses our entire range of $\chi_{\text{CO}_2}^{\text{ini}}$. The hotspot mantle source tends to be even more volatile-rich, up to well over 1000 ppm in CO₂, and several hundred ppm for H₂O (Wallace, 1998; Miller et al., 2019).

Melt concentrations. Our oxidised cases overlap fairly well with estimates of the typical volatile concentrations in modern ridge and hotspot magmas, as well as with the corresponding outgassing fluxes. Simulations that reach higher $\chi_{\text{CO}_2}^{\text{melt}}$ and $\chi_{\text{H}_2\text{O}}^{\text{melt}}$, with respect to modern Earth, accordingly tend to produce higher CO₂ and H₂O outgassing rates. However, for many of our simulations, the mantle is almost completely depleted in volatiles by 700 Myr. Thus even if the convective velocity is increased by a reduction in viscosity, for example, we would not expect outgassing rates to increase any further.

In summary, the most reliable way to attain higher outgassing rates in our stagnant lid model would be to raise the volatile content of the melt. However, a volatile-rich melt is not necessarily attainable by tweaking model parameters because the melt partitioning of CO₂ and H₂O will be ultimately limited by their stocks in the upper mantle source. To illustrate what a stagnant lid regime’s lower interior volatile supplies mean for possible outgassing rates: a mantle with $\chi_{\text{CO}_2}^{\text{ini}} = 180$ ppm and no return fluxes could outgas a maximum of ~ 16 bar CO₂ at 30% depletion and $\chi_{\text{extr}} = 40\%$. Meanwhile, outgassing 8.5 Tmol yr⁻¹ CO₂ (Catling and Kasting, 2017) over 1 Gyr is equivalent to a cumulative ~ 75 bar.

4.2.2. Archean outgassing proxies

Few observational constraints exist on Archean outgassing rates. Xe isotope anomalies in Archean quartz suggest that mantle degassing was about tenfold greater at 3.3 Ga than at present (Avice et al., 2017; Marty et al., 2019). This proxy would apply to C-O-H outgassing rates at 3.3 Ga if they were derived directly from magma production rates—indeed, these high melting rates suggested by Xe isotopes are matched by our stagnant lid model. However, the carbon and water contents of the melt are at least as important as the volume of the melt in determining C-O-H outgassing rates.

4.3. Implications for the Archean Earth system

4.3.1. From outgassing to atmospheric composition

The atmospheric composition and oxidation state do not mimic the volcanic gas composition or oxidation state: photochemical reactions and H escape can oxidise reduced gases, and extraterrestrial impactors could provide significant reducing power (Zahnle et al., 2020). In addition, it is possible that an earlier atmosphere degassed from the magma ocean was in some part still present at the end of the Hadean (Hamano et al., 2013; Nikolaou et al., 2019; Stüeken et al., 2020). We do not model the atmospheric composition here because its complexities deserve more astute attention. However, to build our discussion of this work’s potential implications for the Archean Earth system, we will briefly contextualise our results alongside previous work. We focus on processes affecting the partial pressure of CO₂ due to its importance in long-term climate stability.

The equilibrium between outgassing sources and silicate weathering sinks (seafloor and subaerial) controls $p\text{CO}_2$. Weathering is thought to regulate the surface temperature via a negative feedback loop: in the classic Walker et al. (1981) framework, there would be a single equilibrium combination of $p\text{CO}_2$ and surface temperature for fixed values of the outgassing flux and other relevant parameters (e.g., the weatherable surface area). Lower outgassing—all else being equal—implies a cooler climate, a weaker need to weather, and a lower CO₂ weathering flux (e.g., Kadoya and Tajika, 2014; Krissansen-Totton et al., 2018). For example, Krissansen-Totton et al. (2018) find $p\text{CO}_2$ between 2–500 mbar for a contemporaneous outgassing rate of 3–9 Tmol yr⁻¹ (95% confidence intervals). According to that model, $p\text{CO}_2 < 2$ mbar might therefore be anticipated for less than 3 Tmol yr⁻¹ of outgassing; such rates are not ruled out by this study. Note that this $p\text{CO}_2$ estimate assumes that weathering is not limited by mineral supply, and following equation (29) in Foley and Smye (2018), the supply limit to silicate weathering would only be reached at CO₂ fluxes

well over 100 Tmol yr^{-1} in stagnant lid scenarios (i.e., it is not reached). For comparison, proxy analyses by Hessler et al. (2004) give a lower limit of $p\text{CO}_2 \sim 2.5 \text{ mbar}$ at 3.2 Ga.

4.3.2. Greenhouse warming under the Faint Young Sun

Despite the fainter luminosity of the young sun, geochemical evidence exists for a temperate climate and stable oceans on Earth as early as 4.4 Ga (e.g., Wilde et al., 2001; Valley et al., 2002, 2014). Attempts to explain this paradox often invoke stronger-than-modern atmospheric partial pressures of greenhouse gases (see review in Charnay et al., 2020). Volcanic outgassing, being the main source of these greenhouse gases, is a primary control on steady-state $p\text{CO}_2$ and surface temperature (e.g., Walker et al., 1981; Sleep and Zahnle, 2001; Kadoya and Tajika, 2014; Höning et al., 2019).

Indeed, the CO_2 outgassing rates predicted here are at best several times lower than the values often assumed in Archean Earth climate models (e.g. Sleep and Zahnle, 2001; Wordsworth and Pierrehumbert, 2013; Charnay et al., 2017; Kanzaki and Murakami, 2018; Krissansen-Totton et al., 2018). These higher rates might relate to some combination of a different tectonic mode at the time, a higher ratio of extrusive to intrusive melt, and a more-oxidised mantle.

3D general circulation models can be used to estimate the minimum partial pressures of CO_2 that would provide the necessary greenhouse warming, for a given solar luminosity. For example, Wolf and Toon (2014) find that maintaining 15°C requires $\sim 200 \text{ mbar}$ of CO_2 at 3.8 Ga, if other climate parameters (e.g., day length) are not optimal, and tens of mbar if they are. Note that this smaller value is similar to the minimum $p\text{CO}_2$ from the low-outgassing scenarios studied by Krissansen-Totton et al. (2018). Dedicated atmospheric modelling should estimate the feasibility of greenhouse warming fed by weaker outgassing in the early Archean.

At the least, if a planetary mantle f_{O_2} were below the IW buffer, then it is apparent that virtually no CO_2 could be outgassed in principle, even with melting rates much higher than estimated here. Indeed, silicate Earth may have already reached $f_{\text{O}_2} > \text{IW} + 1$ by the end of the Hadean (Pahlevan et al., 2019). Depending on the longevity of the primordial magma ocean atmosphere, requiring a CO_2 outgassing rate of at least several Tmol yr^{-1} to sustain an early greenhouse may lend a constraint on the timing of mantle oxidation.

5. Conclusions

This work has coupled a 2D numerical model of stagnant lid convection with melting, volatile partitioning into the melt, and chemical speciation of these volatiles. The model returns redox-dependent volcanic outgassing fluxes of CO_2 , CO , H_2O , and H_2 . We have applied this model to Hadean-Archean Earth. We find global CO_2 and H_2O outgassing fluxes on the order of 1 Tmol yr^{-1} and 10 Tmol yr^{-1} respectively, depending on the mantle oxidation state. These fluxes are kept low by the assumption of a stagnant lid regime, wherein outgassing may never be much stronger than predicted here if the upper mantle cannot be efficiently replenished in volatiles. Our model may not apply to a scenario where most outgassing occurred on the seafloor, or where the upper mantle were too oxidised for graphite to be the stable form of carbon.

Coupled convection-outgassing models could inform further studies of the early Earth’s atmospheric evolution. In particular, unknown CO_2 outgassing rates throughout the late Hadean and early Archean account for a significant portion of the uncertainty on the contemporaneous greenhouse warming capacity. Previous estimates of Earth’s climate state during the early period of lower solar luminosity tend to employ outgassing rates higher than the present day, an assumption which might not be substantiated given the unknown tectonic state. If we believe that the presence of surface liquid water in the early Archean demands fairly high CO_2 partial pressures (Charnay et al., 2020), then coupled outgassing models might test whether an early initiation of plate tectonics—combined with rapid mantle oxidation—may be key to building a temperate young planet.

Acknowledgements

This manuscript has been markedly improved by the feedback of two anonymous reviewers. Their effort and their insight were critical in every sense, as were the editor's. The authors would like to thank the HPC Service of ZEDAT, Freie Universität Berlin, for computing time. This work was funded by the Deutsche Forschungsgemeinschaft (DFG, German Research Foundation) – Project-ID 263649064 – TRR 170. This is TRR 170 Publication No. 142. CMG has received additional funding from the University of Cambridge Harding Distinguished Postgraduate Scholars Programme and the Natural Sciences and Engineering Research Council of Canada (NSERC). Cette recherche a été financée par le Conseil de recherches en sciences naturelles et en génie du Canada (CRSNG). CMG thanks R. J. Graham and J. Krissansen-Totton for useful discussion, as well as her PhD supervisors O. Shorttle and J. F. Rudge for their patience with this project.

References

- H. D. Holland, The chemical evolution of the atmosphere and oceans, 1984.
- J. F. Kasting, D. H. Egger, S. P. Raeburn, Mantle redox evolution and the oxidation state of the archaic atmosphere, *The Journal of Geology* 101 (1993) 245–257.
- F. Gaillard, B. Scaillet, A theoretical framework for volcanic degassing chemistry in a comparative planetology perspective and implications for planetary atmospheres, *Earth and Planetary Science Letters* 403 (2014) 307–316.
- K. J. Zahnle, R. Lupu, D. C. Catling, N. Wogan, Creation and Evolution of Impact-generated Reduced Atmospheres of Early Earth, *The Planetary Science Journal* 1 (2020) 11.
- N. Katyal, G. Ortenzi, J. L. Grenfell, L. Noack, F. Sohl, M. Godolt, A. García Muñoz, F. Schreier, F. Wunderlich, H. Rauer, Effect of mantle oxidation state and escape upon the evolution of earth's magma ocean atmosphere, *A&A* 643 (2020) A81.
- N. H. Sleep, K. Zahnle, Carbon dioxide cycling and implications for climate on ancient Earth, *Journal of Geophysical Research* 106 (2001) 1373–1400.
- J. R. Holloway, V. Pan, G. Gudmundsson, High-pressure fluid-absent melting experiments in the presence of graphite: oxygen fugacity, ferric/ferrous ratio and dissolved CO₂, *European Journal of Mineralogy* 4 (1992) 105–114.
- B. J. Wood, M. J. Walter, J. Wade, Accretion of the earth and segregation of its core, *Nature* 441 (2006) 825–833.
- D. Canil, Vanadium partitioning and the oxidation state of archaic komatiite magmas, *Nature* 389 (1997) 842 EP –.
- J. W. Delano, Redox history of the earth's interior since ~3900 Ma: Implications for prebiotic molecules, Origins of life and evolution of the biosphere 31 (2001) 311–341.
- D. Trail, E. B. Watson, N. D. Tailby, The oxidation state of hadean magmas and implications for early earth's atmosphere, *Nature* 480 (2011) 79 EP –.
- R. W. Nicklas, I. S. Puchtel, R. D. Ash, P. M. Piccoli, E. Hanski, E. G. Nisbet, P. Waterton, D. G. Pearson, A. D. Anbar, Secular mantle oxidation across the Archean-Proterozoic boundary: Evidence from V partitioning in komatiites and picrites, *Geochimica et Cosmochimica Acta* 250 (2019) 49 – 75.
- K. Armstrong, D. J. Frost, C. A. McCammon, D. C. Rubie, T. Boffa Ballaran, Deep magma ocean formation set the oxidation state of earth's mantle, *Science* 365 (2019) 903–906.
- V. Debaille, C. O'Neill, A. D. Brandon, P. Haenecour, Q.-Z. Yin, N. Mattielli, A. H. Treiman, Stagnant-lid tectonics in early Earth revealed by 142Nd variations in late Archean rocks, *Earth and Planetary Science Letters* 373 (2013) 83–92.
- M. Brown, T. Johnson, N. J. Gardiner, Plate tectonics and the archaic earth, *Annual Review of Earth and Planetary Sciences* 48 (2020) 291–320.
- L. Noack, M. Godolt, P. von Paris, A.-C. Plesa, B. Stracke, D. Breuer, H. Rauer, Can the interior structure influence the habitability of a rocky planet?, *Planetary and Space Science* 98 (2014) 14–29.
- L. Noack, A. Rivoldini, T. V. Hoolst, Volcanism and outgassing of stagnant-lid planets: Implications for the habitable zone, *Physics of the Earth and Planetary Interiors* 269 (2017) 40 – 57.
- C. O'Neill, A. Lenardic, A. M. Jellinek, W. S. Kiefer, Melt propagation and volcanism in mantle convection simulations, with applications for martian volcanic and atmospheric evolution, *Journal of Geophysical Research: Planets* 112 (2007).
- M. Grott, A. Morschhauser, D. Breuer, E. Hauber, Volcanic outgassing of CO₂ and H₂O on Mars, *Earth and Planetary Science Letters* 308 (2011) 391–400.
- N. Tosi, M. Godolt, B. Stracke, T. Ruedas, J. L. Grenfell, D. Höning, A. Nikolaou, A.-C. Plesa, D. Breuer, T. Spohn, The habitability of a stagnant-lid earth, *Astronomy & Astrophysics* 605 (2017) A71.
- C. Dorn, L. Noack, A. Rozel, Outgassing on stagnant-lid super-earths, *Astronomy & Astrophysics* 614 (2018) A18.
- G. Ortenzi, L. Noack, F. Sohl, C. M. Guimond, J. L. Grenfell, C. Dorn, J. M. Schmidt, S. Vulpius, N. Katyal, D. Kitzmann, H. Rauer, Mantle redox state drives outgassing chemistry and atmospheric composition of rocky planets, *Scientific Reports* 10 (2020) 10907.
- P. Liggins, O. Shorttle, P. B. Rimmer, Can volcanism build hydrogen-rich early atmospheres?, *Earth and Planetary Science Letters* 550 (2020) 116546.
- A. M. Papuc, G. F. Davies, The internal activity and thermal evolution of Earth-like planets, *Icarus* 195 (2008) 447–458.
- E. S. Kite, M. Manga, E. Gaidos, Geodynamics and rate of volcanism on massive earth-like planets, *The Astrophysical Journal* 700 (2009) 1732.
- S. Kadoya, E. Tajika, Evolutionary Climate Tracks of Earth-like Planets, *The Astrophysical Journal Letters* 815 (2015) L7.

- B. J. Foley, P. E. Driscoll, Whole planet coupling between climate, mantle, and core: Implications for rocky planet evolution, *Geochemistry, Geophysics, Geosystems* 17 (2016) 1885–1914.
- B. Charnay, G. L. Hir, F. Fluteau, F. Forget, D. C. Catling, A warm or a cold early earth? new insights from a 3-d climate-carbon model, *Earth and Planetary Science Letters* 474 (2017) 97 – 109.
- J. Krissansen-Totton, G. N. Arney, D. C. Catling, Constraining the climate and ocean pH of the early Earth with a geological carbon cycle model, *Proceedings of the National Academy of Science* 115 (2018) 4105–4110.
- B. J. Foley, A. J. Smye, Carbon Cycling and Habitability of Earth-Sized Stagnant Lid Planets, *Astrobiology* 18 (2018) 873–896.
- J. Krissansen-Totton, D. C. Catling, A coupled carbon-silicon cycle model over earth history: Reverse weathering as a possible explanation of a warm mid-proterozoic climate, *Earth and Planetary Science Letters* 537 (2020) 116181.
- D. Turcotte, On the thermal evolution of the earth, *Earth and Planetary Science Letters* 48 (1980) 53 – 58.
- P. B. Rimmer, O. Shorttle, S. Rugheimer, Oxidised micrometeorites as evidence for low atmospheric pressure on the early earth, *Geochemical Perspectives Letters* 9 (2019) 38–42.
- B. Charnay, E. T. Wolf, B. Marty, F. Forget, Is the faint young sun problem for earth solved?, 2020.
- C. Sagan, G. Mullen, Earth and mars: Evolution of atmospheres and surface temperatures, *Science* 177 (1972) 52–56.
- R. Wordsworth, R. Pierrehumbert, Hydrogen-nitrogen greenhouse warming in earth’s early atmosphere, *Science* 339 (2013) 64–67.
- Y. Kanzaki, T. Murakami, Effects of atmospheric composition on apparent activation energy of silicate weathering: Ii. implications for evolution of atmospheric co₂ in the precambrian, *Geochimica et Cosmochimica Acta* 240 (2018) 314 – 330.
- L. Noack, A. Rivoldini, T. Van Hoolst, Modeling the evolution of terrestrial and water-rich planets and moons, *International Journal On Advances in Systems and Measurements* 9 (2016) 66–76.
- R. F. Katz, M. Spiegelman, C. H. Langmuir, A new parameterization of hydrous mantle melting, *Geochemistry, Geophysics, Geosystems* 4 (2003).
- B. M. French, Some geological implications of equilibrium between graphite and a c-h-o gas phase at high temperatures and pressures, *Reviews of Geophysics* 4 (1966) 223–253.
- J. Holloway, Volatile Interactions in Magmas, pp. 273–293.
- B. Fegley, Chapter 10 - chemical equilibria, in: B. Fegley (Ed.), *Practical Chemical Thermodynamics for Geoscientists*, Academic Press, Boston, 2013, pp. 423 – 508.
- F. Gaillard, B. Scaillet, A theoretical framework for volcanic degassing chemistry in a comparative planetology perspective and implications for planetary atmospheres, *Earth and Planetary Science Letters* 403 (2014) 307–316.
- L. Schaefer, B. Fegley, Redox states of initial atmospheres outgassed on rocky planets and planetesimals, *The Astrophysical Journal* 843 (2017) 120.
- J. W. Hernlund, P. J. Tackley, Modeling mantle convection in the spherical annulus, *Physics of the Earth and Planetary Interiors* 171 (2008) 48 – 54. *Recent Advances in Computational Geodynamics: Theory, Numerics and Applications*.
- G. Schubert, D. L. Turcotte, P. Olson, *Mantle Convection in the Earth and Planets*, Cambridge University Press, 2001.
- S.-i. Karato, P. Wu, Rheology of the upper mantle: A synthesis, *Science* 260 (1993) 771–778.
- P. J. Tackley, M. Ammann, J. P. Brodholt, D. P. Dobson, D. Valencia, Mantle dynamics in super-Earths: Post-perovskite rheology and self-regulation of viscosity, *Icarus* 225 (2013) 50–61.
- J. De Smet, Evolution of the continental upper mantle, Ph.D. thesis, *Geologica Ultraiectina*, 1999.
- E. Ohtani, Y. Nagata, A. Suzuki, T. Kato, Melting relations of peridotite and the density crossover in planetary mantles, *Chemical Geology* 120 (1995) 207 – 221. *Chemical Evolution of the Mantle*.
- M. M. Hirschmann, A. C. Withers, Ventilation of CO₂ from a reduced mantle and consequences for the early Martian greenhouse, *Earth and Planetary Science Letters* 270 (2008) 147–155.
- V. Stagno, Carbon, carbides, carbonates and carbonatitic melts in the Earth’s interior, *Journal of the Geological Society* 176 (2019) 375–387.
- P. Michael, Regionally distinctive sources of depleted morb: Evidence from trace elements and h₂o, *Earth and Planetary Science Letters* 131 (1995) 301 – 320.
- J. C. Afonso, G. Ranalli, M. Fernández, Thermal expansivity and elastic properties of the lithospheric mantle: results from mineral physics of composites, *Physics of the Earth and Planetary Interiors* 149 (2005) 279 – 306.
- C. E. Leshner, F. J. Spera, Chapter 5 - thermodynamic and transport properties of silicate melts and magma, in: H. Sigurdsson (Ed.), *The Encyclopedia of Volcanoes (Second Edition)*, Academic Press, Amsterdam, second edition edition, 2015, pp. 113 – 141.
- J. Valley, W. Peck, E. M. King, S. Wilde, A cool early earth, *Geology* 30 (2002) 351–.
- C. Herzberg, K. Condie, J. Korenaga, Thermal history of the earth and its petrological expression, *Earth and Planetary Science Letters* 292 (2010) 79 – 88.
- L. Elkins-Tanton, Linked magma ocean solidification and atmospheric growth for earth and mars, *Earth and Planetary Science Letters* 271 (2008) 181 – 191.
- P. Barth, L. Carone, R. Barnes, L. Noack, P. Mollière, T. Henning, Magma ocean evolution of the trappist-1 planets, *Astrobiology* 0 (0) null. PMID: 34314604.
- S. Hier-Majumder, M. M. Hirschmann, The origin of volatiles in the earth’s mantle, *Geochemistry, Geophysics, Geosystems* 18 (2017) 3078–3092.
- R. W. Nicklas, I. S. Puchtel, R. D. Ash, Redox state of the archean mantle: Evidence from V partitioning in 3.5–2.4 Ga komatiites, *Geochimica et Cosmochimica Acta* 222 (2018) 447 – 466.
- S. Aulbach, V. Stagno, Evidence for a reducing archean ambient mantle and its effects on the carbon cycle, *Geology* 44 (2016) 751–754.
- J. A. Crisp, Rates of magma emplacement and volcanic output, *Journal of Volcanology and Geothermal Research* 20 (1984)

177–211.

- D. C. Catling, J. F. Kasting, *Volcanic Outgassing and Mantle Redox Evolution*, Cambridge University Press, p. 198–214.
- K. Pahlevan, L. Schaefer, M. M. Hirschmann, Hydrogen isotopic evidence for early oxidation of silicate Earth, *Earth and Planetary Science Letters* 526 (2019) 115770.
- Z. Sharp, F. Mccubbin, C. Shearer, A hydrogen-based oxidation mechanism relevant to planetary formation, *Earth and Planetary Science Letters* 380 (2013) 88–97.
- R. D. Wordsworth, L. K. Schaefer, R. A. Fischer, Redox Evolution via Gravitational Differentiation on Low-mass Planets: Implications for Abiotic Oxygen, Water Loss, and Habitability, *The Astronomical Journal* 155 (2018) 195.
- L. Schaefer, L. T. Elkins-Tanton, Magma oceans as a critical stage in the tectonic development of rocky planets, *Philosophical Transactions of the Royal Society A: Mathematical, Physical and Engineering Sciences* 376 (2018) 20180109.
- M. Ogawa, T. Yanagisawa, Numerical models of martian mantle evolution induced by magmatism and solid-state convection beneath stagnant lithosphere, *Journal of Geophysical Research: Planets* 116 (2011).
- B. Marty, L. Zimmermann, M. Pujol, R. Burgess, P. Philippot, Nitrogen isotopic composition and density of the archaic atmosphere, *Science* 342 (2013) 101–104.
- D. C. Catling, K. J. Zahnle, The archaic atmosphere, *Science Advances* 6 (2020).
- F. Gaillard, B. Scaillet, N. T. Arndt, Atmospheric oxygenation caused by a change in volcanic degassing pressure, *Nature* 478 (2011) 229 EP –.
- C. Zhang, Z. Duan, A model for c–o–h fluid in the earth’s mantle, *Geochimica et Cosmochimica Acta* 73 (2009) 2089–2102.
- D. T. Wetzel, M. J. Rutherford, S. D. Jacobsen, E. H. Hauri, A. E. Saal, Degassing of reduced carbon from planetary basalts, *Proceedings of the National Academy of Sciences* 110 (2013) 8010–8013.
- R. M. Ramirez, R. Kopparapu, M. E. Zugger, T. D. Robinson, R. Freedman, J. F. Kasting, Warming early mars with co₂ and h₂, *Nature Geoscience* 7 (2014) 59–63.
- H. P. Scott, R. J. Hemley, H.-k. Mao, D. R. Herschbach, L. E. Fried, W. M. Howard, S. Bastea, Generation of methane in the earth’s mantle: In situ high pressure–temperature measurements of carbonate reduction, *Proceedings of the National Academy of Sciences* 101 (2004) 14023–14026.
- J. L. Mosenfelder, P. D. Asimow, D. J. Frost, D. C. Rubie, T. J. Ahrens, The mg₂siO₃ system at high pressure: Thermodynamic properties of perovskite, postperovskite, and melt from global inversion of shock and static compression data, *Journal of Geophysical Research: Solid Earth* 114 (2009).
- M. J. Beuchert, H. Schmeling, A melting model for the lowermost mantle using clapeyron slopes derived from experimental data: Consequences for the thickness of ultralow velocity zones (ulvzs), *Geochemistry, Geophysics, Geosystems* 14 (2013) 197–208.
- F. Gaillard, M. A. Bouhifd, E. Füri, V. Malavergne, Y. Marrocchi, L. Noack, G. Ortenzi, M. Roskosz, S. Vulpius, The diverse planetary ingassing/outgassing paths produced over billions of years of magmatic activity, *Space Science Reviews* 217 (2021) 22.
- S. E. Smrekar, E. R. Stofan, N. Mueller, A. Treiman, L. Elkins-Tanton, J. Helbert, G. Piccioni, P. Drossart, Recent hotspot volcanism on venus from virtis emissivity data, *Science* 328 (2010) 605–608.
- P. J. Wallace, Volatiles in subduction zone magmas: concentrations and fluxes based on melt inclusion and volcanic gas data, *Journal of Volcanology and Geothermal Research* 140 (2005) 217 – 240. Energy and Mass Fluxes in Volcanic Arcs.
- E. H. Hauri, E. Cottrell, K. A. Kelley, J. M. Tucker, K. Shimizu, M. L. Voyer, J. Marske, A. E. Saal, Carbon in the convecting mantle, in: B. N. Orcutt, I. Daniel, R. Dasgupta (Eds.), *Deep Carbon: Past to Present*, Cambridge University Press, 2019, p. 237–275.
- W. G. Miller, J. Maclennan, O. Shorttle, G. A. Gaetani, V. Le Roux, F. Klein, Estimating the carbon content of the deep mantle with icelandic melt inclusions, *Earth and Planetary Science Letters* 523 (2019) 115699.
- O. Shorttle, Y. Moussallam, M. E. Hartley, J. Maclennan, M. Edmonds, B. J. Murton, Fe-xanes analyses of reykjanes ridge basalts: Implications for oceanic crust’s role in the solid earth oxygen cycle, *Earth and Planetary Science Letters* 427 (2015) 272 – 285.
- J. M. Tucker, E. H. Hauri, A. J. Pietruszka, M. O. Garcia, J. P. Marske, F. A. Trusdell, A high carbon content of the hawaiian mantle from olivine-hosted melt inclusions, *Geochimica et Cosmochimica Acta* 254 (2019) 156 – 172.
- M. W. Broadley, H. Sumino, D. W. Graham, R. Burgess, C. J. Ballentine, Recycled components in mantle plumes deduced from variations in halogens (cl, br, and i), trace elements, and (3)he/(4)he along the hawaiian-emperor seamount chain, *Geochemistry, geophysics, geosystems : G(3)* 20 (2019) 277–294. GGGE21786[PII].
- M. Le Voyer, E. H. Hauri, E. Cottrell, K. A. Kelley, V. J. M. Salters, C. H. Langmuir, D. R. Hilton, P. H. Barry, E. Füri, Carbon fluxes and primary magma co₂ contents along the global mid-ocean ridge system, *Geochemistry, Geophysics, Geosystems* 20 (2019) 1387–1424.
- B. Marty, I. N. Tolstikhin, Co₂ fluxes from mid-ocean ridges, arcs and plumes, *Chemical Geology* 145 (1998) 233 – 248.
- R. Mjelde, P. Wessel, D. Müller, Global pulsations of intraplate magmatism through the cenozoic, *Lithosphere* 2 (2010) 361–376.
- H. S. O’Neill, A. J. Berry, G. Mallmann, The oxidation state of iron in mid-ocean ridge basaltic (morb) glasses: Implications for their petrogenesis and oxygen fugacities, *Earth and Planetary Science Letters* 504 (2018) 152 – 162.
- H. Amundsen, E.-R. Neumann, Redox control during mantle/melt interaction, *Geochimica et Cosmochimica Acta* 56 (1992) 2405 – 2416.
- R. Dasgupta, M. M. Hirschmann, The deep carbon cycle and melting in earth’s interior, *Earth and Planetary Science Letters* 298 (2010) 1 – 13.
- P. J. Wallace, Water and partial melting in mantle plumes: Inferences from the dissolved h₂o concentrations of hawaiian basaltic magmas, *Geophysical Research Letters* 25 (1998) 3639–3642.

- P. J. Wallace, J. Anderson, Alfred T., Effects of eruption and lava drainback on the H₂O contents of basaltic magmas at Kilauea Volcano, *Bulletin of Volcanology* 59 (1998) 327–344.
- Y. Moussallam, M. Edmonds, B. Scaillet, N. Peters, E. Gennaro, I. Sides, C. Oppenheimer, The impact of degassing on the oxidation state of basaltic magmas: A case study of kilauea volcano, *Earth and Planetary Science Letters* 450 (2016) 317 – 325.
- Y. Moussallam, M.-A. Longpré, C. McCammon, A. Gomez-Ulla, E. F. Rose-Koga, B. Scaillet, N. Peters, E. Gennaro, R. Paris, C. Oppenheimer, Mantle plumes are oxidised, *Earth and Planetary Science Letters* 527 (2019) 115798.
- P. J. Michael, D. W. Graham, The behavior and concentration of CO₂ in the suboceanic mantle: Inferences from undegassed ocean ridge and ocean island basalts, *Lithos* 236 (2015) 338–351.
- G. Avice, B. Marty, R. Burgess, The origin and degassing history of the earth’s atmosphere revealed by archean xenon, *Nature Communications* 8 (2017) 15455.
- B. Marty, D. V. Bekaert, M. W. Broadley, C. Jaupart, Geochemical evidence for high volatile fluxes from the mantle at the end of the Archaean, *Nature* 575 (2019) 485–488. Number: 7783 Publisher: Nature Publishing Group.
- K. Hamano, Y. Abe, H. Genda, Emergence of two types of terrestrial planet on solidification of magma ocean, *Nature* 497 (2013) 607–610.
- A. Nikolaou, N. Katyal, N. Tosi, M. Godolt, J. L. Grenfell, H. Rauer, What factors affect the duration and outgassing of the terrestrial magma ocean?, *The Astrophysical Journal* 875 (2019) 11.
- E. E. Stüeken, S. M. Som, M. Claire, S. Rugheimer, M. Scherf, L. Sproß, N. Tosi, Y. Ueno, H. Lammer, Mission to planet earth: The first two billion years, *Space Science Reviews* 216 (2020) 31.
- J. C. G. Walker, P. B. Hays, J. F. Kasting, A negative feedback mechanism for the long-term stabilization of the earth’s surface temperature, *Journal of Geophysical Research* 86 (1981) 9776–9782.
- S. Kadoya, E. Tajika, Conditions for oceans on earth-like planets orbiting within the habitable zone: Importance of volcanic CO₂ degassing, *The Astrophysical Journal* 790 (2014) 107.
- A. M. Hessler, D. R. Lowe, R. L. Jones, D. K. Bird, A lower limit for atmospheric carbon dioxide levels 3.2 billion years ago, *Nature* 428 (2004) 736–738.
- S. A. Wilde, J. W. Valley, W. H. Peck, C. M. Graham, Evidence from detrital zircons for the existence of continental crust and oceans on the earth 4.4 gyr ago, *Nature* 409 (2001) 175 EP –.
- J. W. Valley, A. J. Cavosie, T. Ushikubo, D. A. Reinhard, D. F. Lawrence, D. J. Larson, P. H. Clifton, T. F. Kelly, S. A. Wilde, D. E. Moser, M. J. Spicuzza, Hadean age for a post-magma-ocean zircon confirmed by atom-probe tomography, *Nature Geoscience* 7 (2014) 219 EP –.
- D. Höning, N. Tosi, T. Spohn, Carbon cycling and interior evolution of water-covered plate tectonics and stagnant-lid planets, *Astronomy and Astrophysics* 627 (2019) A48.
- E. Wolf, O. Toon, Controls on the archean climate system investigated with a global climate model, *Astrobiology* 14 (2014) 241–253. PMID: 24621308.